

The X-ray properties of the dwarf Magellanic-type galaxy NGC 55

A-M. Stobbart, T.P. Roberts, R.S. Warwick

X-ray & Observational Astronomy Group, Dept. of Physics & Astronomy, University of Leicester, Leicester LE1 7RH, U.K.

Submitted

ABSTRACT

We present an analysis of the X-ray properties of the Magellanic-type galaxy NGC 55 based on two contiguous *XMM-Newton* observations. We detect a total of 137 X-ray sources in the field of view, down to a flux of $\sim 5 \times 10^{-15}$ erg cm $^{-2}$ s $^{-1}$ (0.3–6 keV), 42 of which are located within the optical confines of the galaxy. On the basis of X-ray colour classification and after correcting for background objects, we conclude that our source sample includes ~ 20 X-ray binaries, 5 supernova remnants and 7 very soft sources (including 2 good candidate supersoft sources) associated with NGC 55. We also detect an X-ray source coincident with a previously identified globular cluster in NGC 55. Detailed spectral and timing analysis was carried out on 4 of the brightest X-ray sources (excluding the brightest source, which was the subject of a previous paper). One of these objects is identified with a Galactic foreground star and is a possible new RS CVn system. The other three are persistent X-ray sources with X-ray spectra well described by either a single absorbed power-law ($\Gamma \sim 2$) or a multicolour disc blackbody ($kT_{in} \sim 1$ keV) model. While the observed luminosities of these sources ($L_X \sim 1 - 2 \times 10^{38}$ erg s $^{-1}$) and their X-ray spectra are consistent with accreting X-ray binaries, further evidence of short term variability is required to confirm this. Although the *observed* X-ray emission from NGC 55 is dominated by point sources, we do find evidence of an underlying component, which is concentrated on the bar region but has an extent of at least $6'$ (3 kpc) in the plane of the galaxy and $\pm 1'$ (± 500 pc) perpendicular to it. This emission is best fitted by a thermal plasma (MEKAL) ($kT \sim 0.2$ keV) plus power-law ($\Gamma \sim 2$) model but with high intrinsic absorption consistent with its location in the central disc of the galaxy. We interpret the soft component as diffuse thermal emission linked to regions of current star formation, whilst the hard power-law component may originate in unresolved X-ray binary sources. The *intrinsic* luminosity of this residual disc emission may exceed $L_X \sim 6 \times 10^{38}$ erg s $^{-1}$ (0.3–6 keV). A comparison with other Magellanic systems confirms that, in terms of both its discrete X-ray source population and its extended emission, NGC 55 has X-ray properties which are typical of its class.

Key words: galaxies: individual: NGC 55 - galaxies: Magellanic - X-rays: binaries - X-rays: galaxies

1 INTRODUCTION

NGC 55 is a member of the nearby Sculptor Group of galaxies, of which the other prominent members are the starburst galaxy NGC 253 and the spirals NGC 45, NGC 247, NGC 300 and NGC 7793. NGC 55 itself has been classified as a SB(s)m galaxy (de Vaucouleurs 1961) and is viewed almost edge-on with an optical extent of $32.4' \times 5.6'$ (3rd Reference Catalog of Galaxies; de Vaucouleurs et al. 1991). The inclination estimates range from 80° (Hummel, Dettmar, & Wielebinski 1986) to 85° (de Vaucouleurs & Freeman 1972); here we assume a value of 81° (Kiszkurno-Koziej 1988). The optical morphology of NGC 55 is rather asymmetric, with the brightest region displaced $\sim 3'$ from the geometrical centre of the galaxy (Robinson & van Damme

1966). This feature has been interpreted as a bar viewed near to end-on (de Vaucouleurs 1961). Although there is active star formation present throughout much of the disc of NGC 55, the radio continuum emission is concentrated on the bar region and at 6 cm is dominated by a triple source (e.g. Hummel et al. 1986). Recent *Spitzer* far-infrared imaging suggests this is a young (< 2 Myr) star formation complex (Engelbracht et al. 2004). The *Spitzer* observations further imply a global star formation rate of $0.22 M_\odot$ yr $^{-1}$ for NGC 55 (Engelbracht et al. 2004). The edge-on orientation of NGC 55 affords us a prime view of the effects of this disc-based star formation activity on the extra-planar regions. Spectacular ionized gas features, including giant shells and possible galactic chimneys, protrude well above the plane of the galaxy (Ferguson, Wyse, & Gallagher 1996; Otte & Dettmar 1999), sug-

gesting that the star formation powers the ejection of gas from the disc into the halo. At least some of this gas appears to cool sufficiently to form new stars in the halo (Tüllmann et al. 2003; Tüllmann & Rosa 2004).

For such a relatively nearby ($d = 1.78$ Mpc¹), active star-forming system, NGC 55 has been relatively poorly studied at X-ray wavelengths. The first detailed X-ray information came from *ROSAT* PSPC and HRI observations (Read, Ponman & Strickland 1997; Roberts 1997; Schlegel, Barrett & Singh 1997; Dahlem, Weaver & Heckman 1998), revealing a total of 25 sources in and around the galaxy and evidence of localised diffuse emission. Of these sources, 15 were located within the optical confines of the galaxy as defined by the D₂₅ ellipse (Roberts 1997) with one particular source, situated $\sim 7'$ to the east of the main bar complex, found to be several times brighter than any other X-ray source associated with the galaxy. New *XMM-Newton* observations establish this object (XMMU J001528.9-391319) to be an ultraluminous X-ray source (ULX) and, most probably, a black-hole X-ray binary system (Stobbart et al. 2004 - hereafter Paper I). Previous *Chandra* (ACIS-I) observations detect possible extended X-ray emission above the disc of the galaxy, as well as a somewhat brighter diffuse component associated with the disc itself (Oshima et al. 2002).

Here we present a detailed analysis of the *XMM-Newton* observations of NGC 55, focusing on both the properties of the discrete X-ray source population and the underlying diffuse emission. The paper is set out as follows. We first describe the observations and preliminary data reduction techniques (sec. 2). In sec. 3 we give details of the source detection procedure and present a catalogue of the X-ray sources detected in the NGC 55 field. The next three sections consider the X-ray properties of four of the brightest X-ray sources in NGC 55 (sec. 4), the X-ray colours of the full set of detected sources (sec. 5) and the morphology and spectral properties of the faint diffuse X-ray emission observed in NGC 55 (sec. 6). We then discuss the nature of the brightest X-ray sources in NGC 55 and consider the overall X-ray properties of this galaxy in the context of other nearby Magellanic-type systems (sec. 7). Finally, we briefly summarise our results (sec. 8).

2 OBSERVATIONS AND DATA SCREENING

Two observations of NGC 55 were carried out by *XMM-Newton* in the period 2001 November 14-15, with the second observation commencing 2.2 ks after the termination of the first. The pointings were offset in opposite directions with respect to the centre of the galaxy so as to image the full extent of the edge-on galaxy disc (see Table 1).

This paper focuses on data from the EPIC MOS and pn cameras (Turner et al. 2001; Strüder et al. 2001) taken in the full window mode with the thin filter deployed. All the datasets were

¹ The distance to NGC 55 was estimated to be $1.45^{+0.35}_{-0.30}$ Mpc by Graham (1982) based on the apparent magnitude of stars at the tip of the red giant branch (the TRGB method), whereas Pritchett et al. (1987) obtained a value of 1.34 ± 0.08 Mpc, via photometry of carbon stars. More recent estimates, using a variety of techniques, place NGC 55 at a distance of between 1.7 – 2.1 Mpc (Karachentsev et al. 2003; Tikhonov, Galazutdinova, & Drozdovsky 2005; Van de Steene et al. 2004). In the present paper we have taken the distance to NGC 55 to be 1.78 Mpc (Karachentsev et al. 2003).

Table 1. The *XMM-Newton* observations of NGC 55

Obs ID	RA ^a	Dec ^a	Date	UT _{start}
0028740201	00 15 46.0	-39 15 28	2001-11-14	14:20:08
0028740101	00 14 32.9	-39 10 46	2001-11-15	00:24:43

^a Epoch J2000 co-ordinates.

pipeline processed and reduced using standard tools of the *XMM-Newton* Science Analysis Software (SAS) version 5.4.1. After the removal of an interval of soft proton flaring towards the end of the second pointing and utilising only periods when all three cameras (MOS-1, MOS-2 and pn) were in operation, the net exposure times were 30.4 ks and 21.5 ks for the first and second observations respectively.

In the present analysis we use valid pn events with pattern 0-4 but use pattern 0-12 for the MOS cameras. We also exclude events outside the field of view and remove any hot pixels in the data by using the flag expressions #XMMEA_EM and #XMMEA_EP for MOS and pn respectively. We also removed three additional hot columns which remained in the pn data (two in the first observation, and one in the second).

3 X-RAY SOURCES IN THE FIELD OF NGC 55

3.1 Source detection

The first requirement was to produce a list of the discrete X-ray sources detected within the sky area covered by the two *XMM-Newton* observations. For this purpose we combined the MOS-1 and MOS-2 events using the SAS task MERGE and subsequently used the combined MOS (*i.e.*, MOS-1 plus MOS-2) and pn data as separate channels in the source detection process. MOS and pn images were produced for each observation in three energy bands, chosen to provide a good signal-to-noise coverage of the EPIC data: 0.3–1 keV (soft), 1–2 keV (medium) and 2–6 keV (hard), together with the corresponding exposure maps. We believe that these energy bands will provide good signal to noise detections for the sources in the field. Here we use a pixel size of $4'' \times 4''$.

The source detection routines were carried out separately for the MOS and pn datasets over the three energy bands. The SAS task EBOXDETECT was used to perform the initial source detection and employs a sliding box detection method. The task has two different modes of operation, the first of which is the local detection mode in which the images are scanned by a sliding square box, and an object centred in the box is classified as a source if its signal to noise is greater than a specified threshold value². Next, the derived source positions were provided as input for the task ESPLINEMAP which constructs background maps using source-free regions of the image. Once the background maps are available, they are utilised in a further run of EBOXDETECT in ‘map’ mode, leading to an improved detection sensitivity. To complement the sliding-box detection approach we also employed the wavelet search technique via EWAVELET, a method which provides, amongst other advantages, good suppression of multiple false detections in extended sources and is also better at distinguishing close sources. While for

² The signal is derived from the pixel values inside a 5×5 pixel window, and the local background and noise level is estimated from the surrounding 56 pixels (within a full 9×9 pixel window).

EBOXDETECT the source detection was performed simultaneously on the soft, medium and hard datasets for a particular camera and observation, the EWAVELET routine was performed separately on each energy band, detector and observation. Any additional sources detected via the EWAVELET method were added to the EBOXDETECT list. As a final quality check we removed any sources we deemed to be unreliable based on a visual inspection of the image (e.g., unconvincing sources at chip edges or gaps).

The next step was to use the task EMLDETECT to carry out, on a source by source basis, a maximum likelihood fit of the point spread function to the observed spatial distribution of counts measured in the separate energy bands. In this context accurate modelling of the background is essential when determining the significance of a detected source and at this point we used adaptively-smoothed background maps obtained from source-excluded images via the ASMOOTH task. We ran the EMLDETECT task using these improved background maps to produce a standardised set of source parameters. Sources were classified as significant detections if they had a likelihood (DET_ML) value of 10 or more (corresponding to a detection significance of $> 4\sigma$) in at least one of the energy bands, not just the summary band. The final source list was obtained by completing two further iterations of the ASMOOTH and EMLDETECT procedures.

Application of the above procedures resulted in four separate sourcelists (i.e., MOS and pn lists for each observation). We next checked for astrometric offsets by correlating these lists with the USNO A2.0 optical catalogue, using the task EPOSCORR. The derived ‘optimum offsets’ for each observation were used to correct the X-ray source positions to the USNO frame of reference. The final step was to merge the four EMLDETECT source lists into one summary list using the SRCMATCH task, which correlates sources co-located within their 5σ centroiding errors plus a $1''$ systematic.

3.2 The source catalogue

In total, 137 X-ray sources are detected within the field of view encompassed by the two *XMM-Newton* observations, 42 of which are located within the D_{25} ellipse of NGC 55. Fig. 1 shows the broad band (0.3–6 keV) X-ray image obtained by merging the MOS and pn data from the two observations. The positions of the 137 sources which pass the significance test described earlier are marked with circles. Fig. 2 shows the same X-ray source positions overlaid on the optical DSS-2 blue image of the galaxy.

The full X-ray source catalogue appears in Table 2. The table provides the following information:

column 1: The source identification number - sources located within the optical D_{25} ellipse are marked with an asterisk.

column 2-3: The source RA and DEC positions (J2000). The correct IAU designated title for each source can be produced by truncating the coordinates in these columns. For example, Source 1 becomes XMMU J001328.3-390903.

column 4: The 1σ uncertainty in the source position plus a $0.5''$ systematic error.

column 5-7: The measured count rate (corrected for the vignetting) in the pn camera in the soft (S), medium (M) and hard (H) bands. For sources detected in both observations, these count rates are the weighted mean values from the two exposures.

column 8-10: The measured count rate (corrected for the vignetting) in the MOS cameras in the S, M & H bands. Where appropriate, weighted mean values are quoted as for the pn data. Values are quoted for one MOS camera.

column 11-12: Two hardness ratios calculated as $HR1 =$

$(M - S)/(M + S)$ and $HR2 = (H - M)/(H + M)$. For sources detected in more than one instrument or exposure we quote the weighted mean hardness ratios.

column 13: The measured flux in the 0.3–6 keV energy range. The count rate in each detection band was converted to an X-ray flux using Energy Conversion Factors (ECFs) calculated for each instrument from a power-law continuum spectrum with $\Gamma = 1.7$ absorbed by the Galactic foreground column towards NGC 55 ($N_H = 1.55 \times 10^{20} \text{ cm}^{-2}$; Stark et al. 1992). Again, for sources detected in more than one instrument or exposure we took the weighted mean flux values for the particular band. The fluxes derived from the individual bands were subsequently added to provide the quoted instrumental flux (0.3–6 keV).

column 14: The derived X-ray luminosities for sources within the D_{25} ellipse, assuming a distance of 1.78 Mpc.

3.3 X-ray sources associated with NGC 55

Table 3 gives a breakdown of the number of detected sources as a function of instrument and energy band. The D_{25} ellipse of the galaxy occupies ~ 13 per cent of the total field of view, but encompasses ~ 30 per cent of the sources. We have carried out a Monte Carlo simulation to investigate whether the 42 sources detected within the D_{25} ellipse of NGC 55, represent an excess compared to the number of background objects expected by chance. Our predictions are based on the $\log N - \log S$ curves published by Giacconi et al. (2001).

We initially performed a simulation to investigate the source statistics in the medium (1–2 keV) band. Here the comparison was between the number of actual detections in this band and the numbers predicted on the basis of the 0.5–2 keV $\log N - \log S$ relation³. The simulation involved distributing sources over a sky area encompassing the full field of view of the NGC 55 observations with a surface density and flux distribution consistent with a random sampling of the input $\log N - \log S$ curve. The X-ray flux of each simulated source was then converted to counts by folding in the 1–2 keV exposure maps, applying the relevant 0.5–2 keV flux to 1–2 keV counts conversion (assuming the spectral form defined earlier) and finally Poisson deviating the predicted count. A given source was deemed to be ‘detected’ if its estimated count exceeded a threshold value in either the pn or MOS channels (or both) in either of the EPIC observations. The full process involved the determination of the average number of source detections in 5000 simulation runs. The threshold count used in the analysis was set by requiring the number of simulated detections to match the number of actual detections for the off-galaxy regions of the EPIC fields. In practice we found that a threshold of 15 counts gave a reasonable approximation to the detection criteria actually employed in extracting 1-2 keV band sources.

On the basis of this analysis we conclude that in the medium band, the number of sources detected within the D_{25} ellipse of NGC 55 exceeds the source count prediction by 17, that is ~ 55 per cent of the total. However, this must represent a lower limit since the simulation ignores the effect of absorption in the disc of the galaxy, which will tend to suppress the count rates of background sources below the predicted levels. Allowing for column densities within

³ In the simulation we constrained the flux range from which input sources were randomly selected, subject to the $\log N - \log S$ weighting, to be $9 \times 10^{-16} \text{ erg cm}^{-2} \text{ s}^{-1}$ to $2 \times 10^{-13} \text{ erg cm}^{-2} \text{ s}^{-1}$.

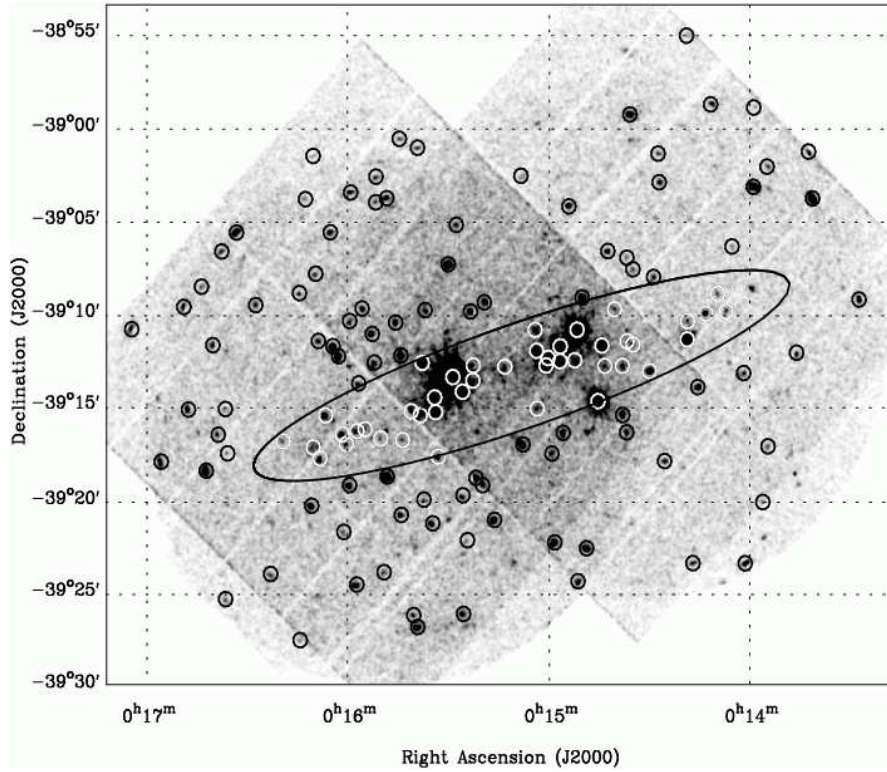


Figure 1. The *XMM-Newton* image of the NGC 55 field in a broad (0.3–6 keV) bandpass. The image has been lightly smoothed using a circular Gaussian mask with $\sigma=1$ pixel (*i.e.*, $4''$). Detected sources are identified with circles. The optical D_{25} ellipse of NGC 55 is also shown.

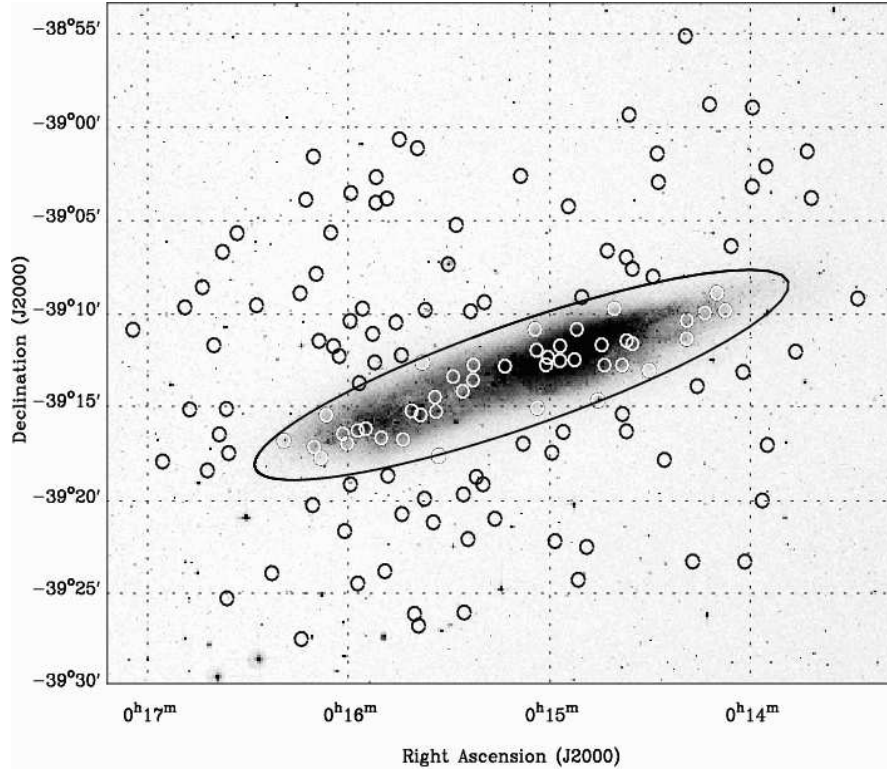


Figure 2. The optical DSS-2 (blue) image of the NGC 55 field with the X-ray source positions marked. The D_{25} ellipse of NGC 55 is also shown.

Table 2. The full catalogue of sources detected in the *XMM-Newton* observations

SRC ID	RA (hh:mm:ss)	DEC ($^{\circ}$: $'$: $''$)	$r_1 \sigma$ ($'$)	pn cts ks $^{-1}$			MOS cts ks $^{-1}$			HR1	HR2	f_X ($\times 10^{-14}$)	L_X ($\times 10^{36}$)
				S	M	H	S	M	H				
1	00:13:28.37	-39:09:03.0	1.14	–	–	–	3.4\pm0.4	3.0\pm0.4	1.4\pm0.4	-0.06 \pm 0.09	-0.36 \pm 0.12	4.63 \pm 0.54	
2	00:13:42.33	-39:03:38.3	0.60	40.5\pm2.8	16.9\pm1.8	14.4\pm1.7	13.2\pm1.1	10.6\pm1.0	7.9\pm0.8	-0.28 \pm 0.05	-0.12 \pm 0.08	17.1 \pm 0.8	
3	00:13:43.61	-39:01:07.2	0.87	17.7\pm2.9	7.4\pm1.8	4.0\pm1.5	4.2\pm0.6	2.2\pm0.5	0.0 \pm 0.1	-0.36 \pm 0.12	-0.88 \pm 0.15	3.01 \pm 0.32	
4	00:13:46.83	-39:11:55.7	1.49	4.3\pm0.8	2.3\pm0.5	1.3\pm0.4	–	–	–	-0.31 \pm 0.13	-0.26 \pm 0.19	1.51 \pm 0.27	
5	00:13:55.16	-39:16:58.4	1.41	2.1\pm0.6	1.2\pm0.3	2.0\pm0.5	0.2 \pm 0.2	0.9\pm0.2	0.4 \pm 0.2	-0.01 \pm 0.19	0.06 \pm 0.23	1.26 \pm 0.21	
6	00:13:55.87	-39:01:56.5	1.28	2.6\pm0.8	1.9\pm0.6	1.0 \pm 0.6	1.3\pm0.3	1.1\pm0.3	0.9 \pm 0.3	-0.12 \pm 0.19	-0.17 \pm 0.27	1.51 \pm 0.27	
7	00:13:56.62	-39:19:58.3	1.36	0.5 \pm 0.4	1.8 \pm 0.6	2.9\pm0.8	0.0 \pm 0.2	0.8 \pm 0.2	1.3\pm0.3	0.73 \pm 0.34	0.23 \pm 0.18	2.01 \pm 0.30	
8	00:13:59.88	-39:03:01.8	0.69	28.7\pm2.0	11.3\pm1.2	6.3\pm1.0	–	–	–	-0.44 \pm 0.05	-0.28 \pm 0.09	8.13 \pm 0.60	
9	00:13:59.90	-38:58:46.0	1.73	4.5\pm1.0	0.0 \pm 0.3	0.0 \pm 0.2	–	–	–	-1.00 \pm 0.13	–	0.45 \pm 0.17	
10	00:14:01.76	-39:23:16.0	0.72	–	–	–	11.8\pm1.0	8.4\pm0.9	4.5\pm0.6	-0.17 \pm 0.07	-0.31 \pm 0.08	14.6 \pm 1.0	
11	00:14:02.49	-39:13:02.5	1.01	3.8\pm0.6	1.4\pm0.3	0.1 \pm 0.2	0.7\pm0.2	0.4 \pm 0.1	0.3 \pm 0.1	-0.42 \pm 0.20	-0.69 \pm 0.24	0.68 \pm 0.10	
12	00:14:06.13	-39:06:14.7	1.91	0.3 \pm 0.3	1.2\pm0.3	0.8 \pm 0.4	–	–	–	0.61 \pm 0.32	-0.20 \pm 0.26	0.68 \pm 0.22	
13*	00:14:07.84	-39:09:44.0	1.24	0.8\pm0.3	1.4\pm0.4	1.2\pm0.3	0.4 \pm 0.2	0.7\pm0.2	0.4 \pm 0.2	0.30 \pm 0.21	-0.17 \pm 0.20	0.99 \pm 0.15	3.76
14*	00:14:10.33	-39:08:47.3	1.53	0.7 \pm 0.4	2.2\pm0.4	0.8 \pm 0.3	0.4 \pm 0.1	0.8\pm0.2	0.3 \pm 0.2	0.40 \pm 0.20	-0.44 \pm 0.20	0.88 \pm 0.15	3.32
15	00:14:12.66	-38:58:36.6	0.96	8.3\pm1.2	3.7\pm0.8	2.4 \pm 0.7	2.7\pm0.6	2.0\pm0.5	2.2\pm0.6	-0.30 \pm 0.16	-0.08 \pm 0.17	3.24 \pm 0.38	
16*	00:14:13.87	-39:09:51.9	0.83	1.4\pm0.4	1.9\pm0.4	2.2\pm0.4	0.5 \pm 0.1	1.9\pm0.2	1.4\pm0.2	0.47 \pm 0.14	-0.06 \pm 0.11	2.07 \pm 0.20	7.85
17	00:14:16.12	-39:13:48.5	0.73	5.8\pm0.7	2.8\pm0.4	1.8\pm0.4	1.8\pm0.2	1.4\pm0.2	1.5\pm0.2	-0.26 \pm 0.11	-0.09 \pm 0.12	2.47 \pm 0.19	
18	00:14:17.33	-39:23:16.4	1.16	3.3\pm0.9	3.8\pm0.8	1.1\pm0.3	2.6\pm0.5	1.5\pm0.4	0.5 \pm 0.3	-0.13 \pm 0.15	-0.53 \pm 0.19	1.75 \pm 0.21	
19*	00:14:19.24	-39:10:16.2	1.22	0.0 \pm 0.2	1.4\pm0.3	1.1\pm0.3	0.3 \pm 0.1	0.4 \pm 0.1	0.7\pm0.2	0.65 \pm 0.26	0.06 \pm 0.18	0.99 \pm 0.15	3.76
20*	00:14:19.31	-39:11:15.2	0.53	27.1\pm1.4	33.3\pm1.5	27.9\pm1.4	8.1\pm0.5	18.4\pm0.8	16.5\pm0.8	0.24 \pm 0.03	-0.07 \pm 0.03	27.0 \pm 0.7	102.4
21	00:14:19.89	-38:54:55.4	2.46	6.5\pm1.4	2.5 \pm 0.9	1.2 \pm 0.9	–	–	–	-0.44 \pm 0.17	-0.35 \pm 0.35	1.71 \pm 0.52	
22	00:14:25.86	-39:17:47.6	1.12	2.7\pm0.5	1.5\pm0.4	1.0 \pm 0.4	1.1\pm0.2	0.8\pm0.2	0.6\pm0.1	-0.23 \pm 0.15	-0.19 \pm 0.19	1.33 \pm 0.14	
23	00:14:27.81	-39:02:48.6	0.94	3.7\pm0.7	1.6\pm0.4	1.6\pm0.4	1.1\pm0.2	1.7\pm0.3	0.8 \pm 0.2	-0.11 \pm 0.13	-0.20 \pm 0.16	1.79 \pm 0.21	
24	00:14:28.17	-39:01:16.1	1.46	3.4\pm0.7	1.3 \pm 0.4	0.4 \pm 0.3	0.9\pm0.2	0.6 \pm 0.2	0.9 \pm 0.3	-0.37 \pm 0.23	-0.06 \pm 0.33	0.98 \pm 0.19	
25	00:14:29.36	-39:07:54.3	1.23	1.4\pm0.4	1.6\pm0.3	0.4 \pm 0.3	0.6\pm0.1	0.6\pm0.1	0.6\pm0.2	0.02 \pm 0.17	-0.20 \pm 0.20	0.87 \pm 0.14	
26*	00:14:30.48	-39:12:57.5	0.69	5.6\pm0.7	3.9\pm0.5	2.2\pm0.4	1.3\pm0.2	2.3\pm0.3	1.1\pm0.2	0.03 \pm 0.09	-0.31 \pm 0.10	2.65 \pm 0.20	10.0
27*	00:14:35.45	-39:11:32.2	1.50	2.2\pm0.5	0.0 \pm 0.2	0.5 \pm 0.3	0.9\pm0.2	0.2 \pm 0.1	0.0 \pm 0.1	-0.85 \pm 0.18	-0.19 \pm 0.69	0.47 \pm 0.10	1.78
28	00:14:35.50	-39:07:29.6	1.66	0.6 \pm 0.3	0.6 \pm 0.3	0.9 \pm 0.3	0.1 \pm 0.1	0.7\pm0.2	0.5 \pm 0.1	0.53 \pm 0.30	-0.06 \pm 0.21	0.76 \pm 0.13	
29	00:14:36.56	-38:59:10.4	1.12	11.4\pm1.4	4.6\pm0.9	1.0 \pm 0.6	4.7\pm0.6	3.5\pm0.5	0.3 \pm 0.3	-0.28 \pm 0.09	-0.78 \pm 0.17	2.97 \pm 0.30	
30*	00:14:37.18	-39:11:22.0	2.26	–	–	–	0.9\pm0.2	0.0 \pm 0.1	0.1 \pm 0.1	-0.92 \pm 0.14	0.53 \pm 0.76	0.52 \pm 0.17	1.98
31	00:14:37.19	-39:16:15.4	1.46	1.6\pm0.4	1.6\pm0.3	0.5 \pm 0.3	–	–	–	-0.03 \pm 0.16	-0.49 \pm 0.22	0.70 \pm 0.17	
32	00:14:37.31	-39:06:52.4	1.38	0.0 \pm 0.1	0.2 \pm 0.2	1.3\pm0.3	0.0 \pm 0.1	0.3 \pm 0.1	1.0\pm0.2	1.00 \pm 0.57	0.65 \pm 0.22	0.96 \pm 0.16	
33	00:14:38.39	-39:15:19.7	0.83	2.7\pm0.4	1.6\pm0.3	1.1\pm0.3	1.1\pm0.2	0.7\pm0.1	0.6\pm0.1	-0.22 \pm 0.11	-0.14 \pm 0.14	1.31 \pm 0.13	
34*	00:14:38.54	-39:12:41.3	1.03	0.7 \pm 0.3	1.8\pm0.4	0.7 \pm 0.3	0.5 \pm 0.1	0.8\pm0.2	0.7\pm0.2	0.33 \pm 0.17	-0.25 \pm 0.17	0.95 \pm 0.14	3.62
35*	00:14:40.88	-39:09:38.6	1.42	–	–	–	0.5 \pm 0.1	0.9\pm0.2	0.7\pm0.2	0.33 \pm 0.16	-0.14 \pm 0.16	1.58 \pm 0.27	5.98
36	00:14:42.95	-39:06:31.0	0.85	0.0 \pm 0.2	2.9\pm0.5	3.3\pm0.5	0.2 \pm 0.1	1.6\pm0.3	2.3\pm0.3	0.90 \pm 0.13	0.13 \pm 0.11	2.84 \pm 0.25	
37*	00:14:43.74	-39:12:41.5	1.49	0.2 \pm 0.3	1.2\pm0.3	0.9 \pm 0.3	0.1 \pm 0.1	0.7\pm0.2	0.3 \pm 0.2	0.72 \pm 0.31	-0.25 \pm 0.22	0.73 \pm 0.14	2.78
38*	00:14:44.62	-39:11:35.9	0.58	6.7\pm0.6	10.1\pm0.7	8.7\pm0.6	2.1\pm0.2	4.8\pm0.4	4.3\pm0.3	0.30 \pm 0.05	-0.07 \pm 0.05	7.68 \pm 0.30	29.1
39	00:14:45.73	-39:14:35.3	0.51	198.5\pm2.9	64.0\pm1.6	9.8\pm0.7	51.2\pm1.0	25.1\pm0.7	3.6\pm0.3	-0.45 \pm 0.01	-0.73 \pm 0.02	35.9 \pm 0.4	
40	00:14:49.00	-39:22:29.9	0.82	1.8 \pm 0.6	6.3\pm1.0	2.3\pm0.7	1.0\pm0.2	2.3\pm0.2	2.1\pm0.2	0.45 \pm 0.08	-0.11 \pm 0.10	3.42 \pm 0.27	
41	00:14:50.55	-39:09:01.0	0.62	8.8\pm0.7	4.9\pm0.5	2.7\pm0.4	3.1\pm0.5	3.0\pm0.4	2.5\pm0.4	-0.23 \pm 0.10	-0.22 \pm 0.08	3.47 \pm 0.22	
42	00:14:51.52	-39:24:16.1	0.88	–	–	–	3.6\pm0.4	2.5\pm0.3	1.0\pm0.2	-0.19 \pm 0.08	-0.42 \pm 0.11	4.06 \pm 0.39	
43*	00:14:52.02	-39:10:45.2	0.50	106.0\pm2.1	119.6\pm2.3	53.3\pm1.6	32.3\pm0.8	56.5\pm1.1	25.6\pm0.8	0.16 \pm 0.01	-0.38 \pm 0.01	64.0 \pm 0.7	242.8
44*	00:14:52.68	-39:12:23.9	1.26	–	–	–	1.0\pm0.2	0.8\pm0.2	0.4 \pm 0.2	-0.11 \pm 0.17	-0.30 \pm 0.20	1.39 \pm 0.26	5.26
45	00:14:54.54	-39:04:07.4	0.85	5.6\pm0.8	3.2\pm0.6	0.5 \pm 0.3	2.6\pm0.4	2.3\pm0.3	0.2 \pm 0.2	-0.16 \pm 0.10	-0.77 \pm 0.16	1.70 \pm 0.18	
46	00:14:56.04	-39:16:17.9	0.84	3.0\pm0.4	1.9\pm0.3	1.1 \pm 0.3	0.5 \pm 0.1	0.8\pm0.1	0.4\pm0.1	-0.04 \pm 0.11	-0.27 \pm 0.13	1.15 \pm 0.11	
47*	00:14:57.00	-39:11:39.2	0.51	20.3\pm1.0	42.2\pm1.3	37.2\pm1.3	6.3\pm0.4	20.0\pm0.6	17.8\pm0.6	0.44 \pm 0.02	-0.05 \pm 0.02	31.6 \pm 0.6	119.7
48*	00:14:57.04	-39:12:26.8	1.54	2.6\pm0.6	1.3 \pm 0.4	0.2 \pm 0.2	0.8 \pm 0.2	0.5 \pm 0.2	0.1 \pm 0.1	-0.29 \pm 0.20	-0.75 \pm 0.32	0.59 \pm 0.12	2.25
49	00:14:58.48	-39:22:11.1	0.69	7.0\pm0.8	2.2\pm0.4	1.7\pm0.3	1.1\pm0.2	1.4\pm0.2	0.6\pm0.1	-0.30 \pm 0.08	-0.26 \pm 0.12	1.99 \pm 0.16	
50	00:14:59.39	-39:17:24.9	1.32	0.3 \pm 0.3	0.8 \pm 0.3	1.4\pm0.4	0.0 \pm 0.0	0.5\pm0.1	0.5\pm0.1	0.87 \pm 0.17	0.12 \pm 0.20	0.91 \pm 0.14	
51*	00:15:00.62	-39:12:16.4	1.16	–	–	–	0.4 \pm 0.1	0.7\pm0.1	0.8\pm0.1	0.31 \pm 0.15	-0.04 \pm 0.12	1.74 \pm 0.22	6.58
52*	00:15:01.18	-39:12:40.6	0.98	5.0\pm0.6	1.6\pm0.3	0.2 \pm 0.2	1.4\pm0.2	0.5 \pm 0.2	0.2 \pm 0.1	-0.49 \pm 0.12	-0.72 $\pm</$		

SRC ID	RA (hh:mm:ss)	DEC (° : ' : ")	$r_{1\sigma}$ (")	pn cts ks ⁻¹			MOS cts ks ⁻¹			HR1	HR2	f_X ($\times 10^{-14}$)	L_X ($\times 10^{36}$)
				S	M	H	S	M	H				
70	00:15:27.91	-39:05:07.7	1.28	2.8±0.5	0.3±0.2	0.1±0.2	0.5±0.2	0.4±0.2	0.0±0.0	-0.68±0.14	-0.95±0.61	0.40±0.08	
71*	00:15:28.87	-39:13:18.7	0.50	833.6±5.9	772.8±5.8	225.1±3.2	110.6±1.9	158.8±2.3	43.9±1.2	0.04±0.01	-0.52±0.01	247.3±1.5	937.6
72	00:15:30.29	-39:07:15.0	0.72	2.3±0.5	2.7±0.5	4.4±0.6	0.6±0.1	1.5±0.2	3.1±0.3	0.28±0.13	0.32±0.08	4.04±0.27	
73*	00:15:33.18	-39:17:35.3	1.13	1.0±0.3	1.0±0.2	0.7±0.2	0.4±0.1	0.2±0.1	0.2±0.1	-0.12±0.21	-0.10±0.26	0.62±0.10	2.33
74*	00:15:33.98	-39:15:12.2	0.67	9.9±0.7	2.7±0.4	0.6±0.3	2.0±0.2	1.4±0.2	0.0±0.1	-0.44±0.06	-0.87±0.13	1.59±0.11	6.02
75*	00:15:34.27	-39:14:24.8	0.52	27.6±1.1	35.1±1.2	30.0±1.1	6.2±0.3	13.2±0.5	11.7±0.5	0.24±0.03	-0.07±0.03	24.5±0.5	93.0
76	00:15:34.80	-39:21:10.4	1.00	2.1±0.4	2.5±0.4	2.7±0.4	0.3±0.1	0.8±0.1	0.3±0.1	0.29±0.13	-0.19±0.11	1.13±0.11	
77	00:15:37.13	-39:09:42.7	1.35	2.3±0.4	0.5±0.2	0.1±0.2	-	-	-	-0.67±0.10	-0.82±0.39	0.37±0.10	
78	00:15:37.43	-39:19:54.1	1.58	0.4±0.3	1.0±0.2	0.2±0.2	0.4±0.1	0.2±0.1	0.0±0.0	-0.02±0.28	-0.77±0.36	0.26±0.06	
79*	00:15:38.00	-39:12:32.8	0.69	3.7±0.4	3.1±0.4	1.4±0.3	1.1±0.1	1.4±0.2	0.9±0.1	0.02±0.08	-0.27±0.09	1.91±0.13	7.22
80*	00:15:38.54	-39:15:22.5	1.71	1.3±0.3	2.3±0.4	1.2±0.3	-	-	-	0.27±0.14	-0.31±0.13	1.17±0.18	4.42
81	00:15:39.24	-39:26:44.9	0.83	8.9±1.0	3.3±0.6	3.0±0.6	2.0±0.3	1.2±0.2	1.4±0.3	-0.38±0.09	0.01±0.14	3.15±0.26	
82	00:15:39.41	-39:00:59.0	1.50	5.4±1.0	4.9±0.8	1.5±0.7	-	-	-	-0.05±0.13	-0.53±0.18	2.13±0.43	
83	00:15:40.45	-39:26:06.5	1.25	2.4±0.6	1.5±0.4	0.8±0.4	0.7±0.2	0.6±0.2	0.3±0.1	-0.15±0.17	-0.31±0.25	0.98±0.16	
84*	00:15:41.26	-39:15:09.3	1.15	3.8±0.6	0.7±0.3	0.0±0.1	0.7±0.1	0.2±0.1	0.0±0.0	-0.66±0.14	-0.98±0.33	0.42±0.06	1.58
85*	00:15:43.82	-39:16:41.8	2.27	1.4±0.3	0.1±0.1	0.0±0.1	-	-	-	-0.93±0.13	-1.00±3.57	0.15±0.06	0.58
86	00:15:44.17	-39:20:43.5	0.94	2.8±0.4	1.5±0.3	0.7±0.2	0.5±0.1	0.4±0.1	0.2±0.1	-0.22±0.14	-0.37±0.17	0.78±0.10	
87	00:15:44.28	-39:12:09.2	0.72	6.6±1.2	3.1±0.8	2.7±0.8	1.7±0.2	1.8±0.2	1.0±0.1	-0.06±0.14	-0.27±0.17	2.79±0.19	
88	00:15:44.79	-39:00:32.4	1.09	3.7±0.9	5.5±1.0	2.4±0.7	-	-	-	0.20±0.15	-0.39±0.15	2.58±0.44	
89	00:15:45.87	-39:10:23.0	0.96	2.5±0.4	1.0±0.2	0.9±0.3	0.3±0.1	0.4±0.1	0.3±0.1	-0.20±0.12	-0.09±0.17	0.84±0.11	
90	00:15:48.35	-39:18:39.3	0.59	11.9±0.8	6.3±0.5	2.8±0.4	3.3±0.3	2.3±0.2	1.3±0.2	-0.26±0.06	-0.33±0.07	3.93±0.19	
91	00:15:48.54	-39:03:42.0	1.08	4.4±0.7	2.9±0.6	1.0±0.5	1.7±0.3	1.1±0.3	0.5±0.2	-0.20±0.14	-0.43±0.21	1.65±0.23	
92	00:15:49.27	-39:23:48.2	1.47	0.9±0.3	0.5±0.3	0.8±0.3	0.3±0.1	0.5±0.1	0.3±0.1	0.11±0.29	-0.15±0.24	0.67±0.13	
93*	00:15:50.29	-39:16:36.8	2.24	1.2±0.3	0.0±0.1	0.0±0.1	-	-	-	-1.00±0.18	-	0.12±0.05	0.47
94	00:15:51.69	-39:02:32.5	1.53	1.3±0.5	1.6±0.5	2.6±0.6	0.3±0.2	1.1±0.3	0.7±0.3	0.39±0.23	0.05±0.20	1.69±0.26	
95	00:15:51.79	-39:03:55.4	1.34	0.6±0.5	1.7±0.5	1.9±0.6	0.1±0.1	0.1±0.1	1.2±0.3	0.40±0.32	0.46±0.20	1.52±0.26	
96	00:15:52.19	-39:12:32.1	1.31	0.9±0.3	1.0±0.2	0.9±0.3	-	-	-	0.08±0.18	-0.04±0.18	0.76±0.15	
97	00:15:52.80	-39:10:59.8	0.87	3.1±0.5	1.0±0.3	0.9±0.3	0.6±0.1	0.6±0.1	0.4±0.1	-0.33±0.11	-0.17±0.19	1.00±0.11	
98*	00:15:54.92	-39:16:06.9	1.34	0.5±0.3	0.7±0.2	0.4±0.2	0.0±0.1	0.0±0.0	0.5±0.1	0.16±0.31	-0.23±0.30	0.52±0.10	1.96
99	00:15:55.83	-39:09:37.8	1.02	3.2±0.5	1.4±0.3	0.4±0.2	1.4±0.4	0.6±0.2	0.6±0.2	-0.38±0.19	-0.38±0.24	0.87±0.13	
100	00:15:56.82	-39:13:39.5	1.06	0.1±0.1	0.8±0.2	2.1±0.4	0.0±0.0	0.3±0.1	0.4±0.1	0.97±0.12	0.32±0.16	0.84±0.11	
101*	00:15:57.33	-39:16:12.9	1.14	3.7±0.5	0.3±0.2	0.0±0.1	0.7±0.1	0.0±0.1	0.0±0.0	-0.87±0.11	-1.00±1.00	0.38±0.05	1.44
102	00:15:57.40	-39:24:27.9	0.79	5.6±0.7	2.1±0.4	1.2±0.4	1.8±0.2	0.7±0.2	0.7±0.2	-0.46±0.10	-0.13±0.17	1.73±0.16	
103	00:15:59.24	-39:03:23.8	1.00	6.8±1.0	2.2±0.6	1.3±0.5	2.2±0.4	0.8±0.2	0.7±0.2	-0.50±0.14	-0.13±0.22	1.94±0.24	
104	00:15:59.52	-39:10:18.1	1.56	1.9±0.4	1.1±0.3	0.7±0.3	-	-	-	-0.27±0.15	-0.23±0.22	0.76±0.16	
105	00:15:59.54	-39:19:07.2	0.74	4.1±0.5	2.8±0.4	1.3±0.3	0.9±0.2	1.0±0.1	0.6±0.1	-0.09±0.10	-0.34±0.12	1.55±0.13	
106*	00:16:00.50	-39:16:55.0	1.45	0.0±0.1	0.5±0.2	1.7±0.3	0.0±0.0	0.1±0.1	0.4±0.1	0.85±0.51	0.55±0.21	0.73±0.11	2.78
107	00:16:01.26	-39:21:38.3	1.61	0.4±0.3	0.5±0.2	0.9±0.3	0.0±0.1	0.2±0.1	0.4±0.1	0.50±0.38	0.26±0.25	0.62±0.11	
108*	00:16:01.75	-39:16:23.1	0.75	0.2±0.1	0.5±0.2	5.1±0.5	0.0±0.0	0.1±0.1	2.1±0.2	0.57±0.40	0.86±0.06	2.93±0.21	11.1
109	00:16:02.79	-39:12:11.5	0.62	9.8±0.7	4.9±0.5	2.4±0.4	2.0±0.2	2.0±0.2	1.3±0.2	-0.21±0.07	-0.27±0.08	3.27±0.18	
110	00:16:04.47	-39:11:39.4	0.63	6.3±0.6	5.2±0.5	2.7±0.4	2.3±0.3	2.1±0.3	1.6±0.2	-0.07±0.08	-0.24±0.09	3.34±0.20	
111	00:16:05.24	-39:05:31.8	1.05	1.3±0.4	3.2±0.6	2.2±0.5	0.4±0.2	1.8±0.3	1.3±0.3	0.52±0.15	-0.18±0.14	2.15±0.25	
112*	00:16:06.67	-39:15:22.5	0.86	1.2±0.3	2.0±0.3	2.6±0.4	0.2±0.1	0.9±0.2	1.0±0.2	0.41±0.16	0.08±0.12	1.85±0.17	7.03
113*	00:16:08.34	-39:17:41.1	0.87	2.1±0.4	3.4±0.5	2.1±0.4	0.5±0.1	1.0±0.2	0.3±0.1	0.27±0.12	-0.35±0.12	1.32±0.13	5.02
114	00:16:08.81	-39:11:22.2	1.15	1.7±0.4	0.8±0.2	0.7±0.3	0.5±0.1	0.5±0.1	0.2±0.1	-0.23±0.16	-0.19±0.23	0.70±0.11	
115	00:16:09.59	-39:07:45.4	1.90	1.9±0.4	1.2±0.3	0.0±0.2	-	-	-	-0.24±0.16	-1.00±0.28	0.37±0.11	
116	00:16:10.33	-39:01:25.6	2.45	2.4±0.6	0.8±0.5	1.5±0.6	-	-	-	-0.48±0.24	0.28±0.32	1.20±0.36	
117*	00:16:10.37	-39:17:05.3	2.80	1.0±0.4	1.2±0.3	0.0±0.1	-	-	-	0.06±0.22	-0.92±0.19	0.31±0.09	1.18
118	00:16:10.81	-39:20:13.7	0.76	4.5±0.6	3.4±0.5	1.9±0.4	0.6±0.1	1.0±0.2	1.0±0.2	-0.02±0.13	-0.16±0.13	2.06±0.18	
119	00:16:12.59	-39:03:45.0	2.79	2.1±0.6	0.3±0.4	0.8±0.5	-	-	-	-0.74±0.26	0.45±0.50	0.73±0.28	
120	00:16:14.28	-39:27:27.3	1.62	-	-	-	0.5±0.2	0.9±0.2	0.8±0.2	0.24±0.23	-0.02±0.18	1.73±0.33	
121	00:16:14.39	-39:08:48.1	1.24	0.6±0.3	1.5±0.3	0.6±0.3	0.6±0.1	0.4±0.1	0.3±0.1	0.15±0.22	-0.32±0.24	0.72±0.14	
122*	00:16:19.34	-39:16:45.5	2.61	0.2±0.2	1.3±0.3	0.5±0.3	-	-	-	0.75±0.26	-0.48±0.24	0.46±0.15	1.76
123	00:16:23.06	-39:23:53.7	1.75	2.2±0.5	0.9±0.3	0.4±0.3	-	-	-	-0.43±0.18	-0.42±0.37	0.57±0.18	
124	00:16:27.39	-39:09:26.6	1.66	1.4±0.4	1.6±0.4	0.7±0.4	-	-	-	0.08±0.20	-0.42±0.25	0.75±0.21	
125	00:16:33.07	-39:05:32.6	0.73	13.6±1.4	6.1±1.0	3.7±0.7	4.9±0.6	3.3±0.5	1.4±0.4	-0.30±0.08	-0.33±0.12	4.72±0.36	
126	00:16:35.81	-39:17:24.4	1.39	2.0±0.4	0.0±0.1	0.3±0.3	-	-	-	-1.00±0.08	1.00±0.53	0.36±0.15	
127	00:16:36.45	-39:15:01.5	2.17	-	-	-	0.1±0.1	0.7±0.2	0.0±0.1	0.78±0.22	-1.00±0.22	0.35±0.14	
128	00:16:36.48	-39:25:14.6	1.45	-	-	-	1.9±0.4	0.9±0.3	0.8±0.2	-0.36±0.15	-0.04±0.20	2.33±0.38	
129	00:16:37.43	-39:06:33.3	1.47	3.8±0.9	2.1±0.6	1.2±0.6	-	-	-	-0.29±0.17	-0.29±0.26	1.37±0.35	
130	00:16:38.59	-39:16:24.1	1.42	2.3±0.5	1.9±0.4	0.6±0.3	-	-	-	-0.11±0.15	-0.54±0.22	0.84±0.20	
131	00:16:40.12	-39:11:35.3	1.19	3.4±0.6	2.2±0.5	0.8±0.4	1.0±0.2	0.9±0.2	0.3±0.2	-0.15±0.15	-0.47±0.23	1.16±0.19	
132	00:16:42.18	-39:18:20.2	0.70	11.0±1.1	7.3±0.9	5.0±0.8	2.3±0.3	3.4±0.4	2.9±0.4	-0.04±0.08	-0.14±0.09	5.54±0.35	
133	00:16:43.46	-39:08:26.8	1.84	0.2±0.3	2.0±0.5	1.3±0.5	-	-	-	0.86±0.28	-0.23±0.22	1.02±0.29	
134	00:16:47.41	-39:15:02.9	1.13	4.0±0.7	3.2±0.6	0.9±0.5	1.2±0.3	1.0±0.3	1.6±0.3	-0.10±0.16	-0.11±0.17	1.82±0.24	
135	00:16:48.71	-39:09:32.0	0.97	6.0±1.0	4.3±0.8	1.1±0.5	1.5±0.4	1.3±0.3	1.1±0.3	-0.14±0.18	-0.37±0.17	2.14±0.27	
136	00:16:55.54	-39:17:50.6	1.11	6.1±0.9	3.9±0.7	2.4±0.7	2.1±0.4	1.3±0.3	1.7±0.4	-0.23±0.14	-0.06±0.16	2.93±0.32	
137	00:17:04.21	-39:10:43.4	1.09	12.6±1.6	5.9±1.0	2.7±0.8	-	-	-	-0.36±0.09	-0.36±0.15		

the disc of NGC 55 of up to 10^{22} cm^{-2} , we estimate that the above fraction should be increased by a further 5 – 10 per cent, implying that roughly two-thirds of the medium band sources within the D_{25} ellipse are probably associated with the galaxy. These sources presumably comprise the bright end of the intrinsic X-ray source population of NGC 55.

The extension of the above analysis to the soft band is complicated by the increased impact of the absorption in the disc of NGC 55. For the hard band, similar results to the above were obtained, albeit with poorer statistics. However, we consider that few of the D_{25} sources detected solely in the soft band are likely to be background objects given the softness of their spectra, whereas the hard-band only detections represent just a few sources in total. In summary, we estimate that there may be 10-15 background interlopers in the sample of 42 sources detected within the D_{25} ellipse of NGC 55.

3.4 Cross-correlation with other catalogues

We have cross-correlated the current source list with other multi-wavelength data, including the catalogues available in the NED and SIMBAD databases, by searching for matches within the 3σ error radius (including a $1''$ systematic error) of each *XMM* source position. The results are summarised in Table 4. Of the 14 sources with possible identifications, 6 lie within the confines of the D_{25} ellipse of NGC 55. Four of these are likely to be objects within the galaxy itself, *i.e.*, sources 48, 52 and 58 which coincide with radio sources and have hardness ratios commensurate with supernova remnants (see sec. 5), and source 71, a likely black-hole X-ray binary system in NGC 55 (Paper I). The other two ‘identified’ D_{25} sources are classed optically as galaxies and are presumably background Active Galactic Nuclei (AGN). Of the remaining 8 identified sources, 6 are similarly associated with background galaxies, whilst source 90, which lies just outside the D_{25} ellipse, is coincident with a possible globular cluster located in the halo of NGC 55 (Liller & Alcaino 1983; Olsen et al. 2004) and source 39 is coincident with a variable (foreground) star. Fig. 3 shows the central part of the 0.3 – 6 keV *XMM-Newton* image with sources of interest marked with different symbols.

Table 4 also lists the matches between the *XMM-Newton* sources and previous *ROSAT* X-ray source detections (again within a 3σ position error, but also incorporating $15/10''$ systematic uncertainties in the *ROSAT* PSPC/HRI data respectively). A total of 15 X-ray sources within the D_{25} ellipse have previously been catalogued by *ROSAT*, as have 12 outside this region. Finally, we performed a brief comparison of these sources to the NGC 55 source list from the *Chandra* observation (Obs ID 2255), produced via the standard CIAO processing tools. From this comparison we found that our *XMM-Newton* sources 29, 34, 55 and 56 are potentially subject to source confusion, as they could be resolved into two separate sources by the sub-arcsecond spatial resolution of *Chandra*.

4 THE BRIGHTEST DISCRETE X-RAY SOURCES

Six catalogued sources with observed fluxes in excess of $10^{-13} \text{ erg cm}^{-2} \text{ s}^{-1}$ lie within or close to the D_{25} ellipse of NGC 55. These sources (20, 39, 43, 47, 71 and 75 in Table 2) have been detected with sufficiently high count rates to permit reasonably detailed spectral and temporal analyses of their X-ray properties. We presented a study of the brightest source (71) in Paper I. Here,

Table 3. The number of sources detected in each energy band in the pn and MOS images.

Camera	Energy Band			
	SOFT	MEDIUM	HARD	S/M/H
pn	25[91]	25[93]	18[55]	35[119]
MOS	19[70]	22[83]	20[64]	32[103]
pn/MOS	29[105]	30[110]	23[76]	42[137]

NOTES: The numbers quoted are for the D_{25} ellipse with the full-field values given in square brackets. The total number of individual sources detected in various instrument and energy band combinations is also indicated.

we analyse four of the next five brightest sources, excluding only source 75 for reasons of practicality. The emission from this latter source was contaminated by the wings of the point spread function (PSF) of source 71 in both observations (and furthermore it lay at the very edge of the field of view in the second observation, where it was detected only in the MOS data). We do include source 20, although it was only within the field of view in the second observation, and source 39 which as previously noted may be identified with a foreground star.

4.1 Light curves

We extracted background-subtracted light curves for each source based on the combined 0.3 – 6 keV data from the three EPIC cameras. For sources 20 and 47 we used circular source extraction apertures with radii of $35''$. For the marginally-brighter sources 39 and 43, we used extraction regions with a $40''$ radius. The background data were extracted from same-sized apertures, positioned in the nearest source-free regions visible in all three detectors. We show the resulting light curves with 200 s time binning in Fig. 4. In each case we correct the count rate from each observation for vignetting effects so as to plot the equivalent on-axis count rate.

We have investigated the short-term X-ray variability of each source by carrying out a χ^2 test (against the hypothesis of a constant flux) on the raw 200 s binned light curves. We also performed a Kolmogorov-Smirnov (K-S) test to search for additional variability characteristics, such as low amplitude underlying trends in the light curve, that a χ^2 test might not detect. For the latter purpose we used only the pn light curves with 1s time bins. The results of both tests are summarised in Table 5. It appears that source 39 (the foreground star) is the only object in the set for which there is strong evidence for short-term X-ray variability (greater than 99.9 per cent probability in each test). Of the three remaining sources, sources 20 and 47 show limited evidence (at $\gtrsim 2\sigma$ significance) of variability in one of the tests. However, source 43 shows no evidence at all of short-term variability.

All four sources were also previously detected in both the *ROSAT* PSPC (performed on 22 – 24 November 1992) and HRI (12 – 14 December 1994) observations indicating that these are all relatively persistent sources. A comparison of the measured X-ray fluxes (based on the simple spectral models derived in the next section) reveals that sources 20, 39 and 43 varied by factors of ~ 2 , ~ 2 and ~ 3 respectively, but that the flux of source 47 remained remarkably steady at $1.4 \pm 0.2 \times 10^{-13} \text{ erg cm}^{-2} \text{ s}^{-1}$ (0.5 – 2 keV) over the 9-yr baseline.

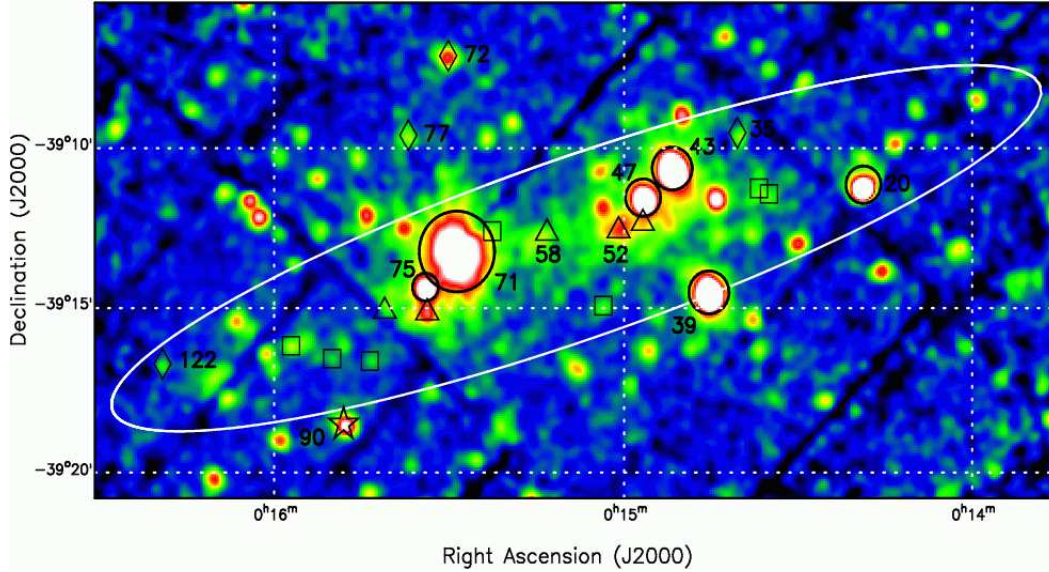


Figure 3. The central regions of the *XMM-Newton* image of the NGC 55 field in a broad (0.3 – 6 keV) bandpass. The ellipse marks the optical extent of the galaxy as measured by the D_{25} isophote. The six brightest X-ray sources are highlighted with circles denoting the spectral extraction radius used. The triangles mark the positions of sources with hardness ratios commensurate with SNRs, whereas the squares mark very soft sources (see sec. 5). An X-ray source possibly located within a globular cluster (Beasley & Sharples 2000) lies at the position of the star symbol. Sources identified with background galaxies are indicated by diamonds.

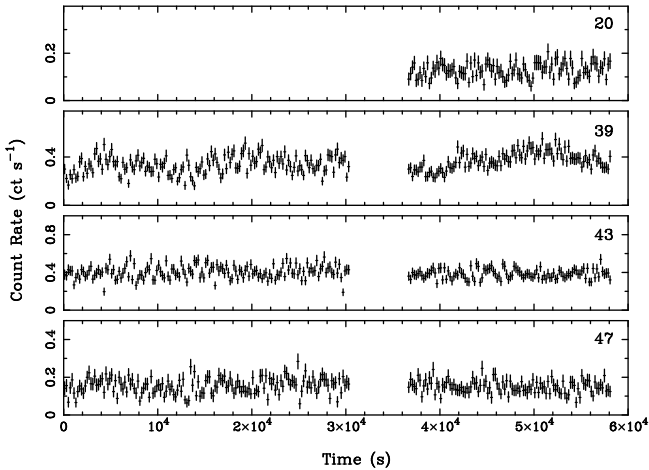


Figure 4. The background-subtracted 0.3 – 6 keV light curves of four bright sources, displayed in 200 s time bins. The light curves are based on the combined data from the MOS-1, MOS-2 and pn cameras. The error bars correspond to $\pm 1\sigma$.

4.2 X-ray Spectra

X-ray spectra were extracted in the 0.3 – 10 keV band, using circular extraction apertures with radii of $35''$ (sources 20 and 47) or $40''$ (sources 39 and 43) (cf. Fig. 3). Background data were again extracted from nearby source-free regions, in this case with radii of $50''$ for sources 39 and 43, and $60''$ for sources 20 and 47; as far as possible, we chose regions located at similar distances from the pn readout nodes to the sources, and free of diffuse emission from the galaxy - see sec. 6. We used the SAS task ESPECGET to produce a source and background spectrum together with the Ancillary Response File (ARF) and Redistribution Matrix File (RMF) required

Table 5. Tests for short-term variability

Source	χ^2 statistic		K-S statistic
	χ^2/dof	$P_{\chi^2}(\text{var})$	$P_{K-S}(\text{var})$
Obs 1			
39	228.5/151	> 99.9 per cent	> 99.9 per cent
43	155.2/151	–	–
47	153.2/151	–	98 per cent
Obs 2			
20	137.3/107	97 per cent	–
39	274.5/107	> 99.9 per cent	> 99.9 per cent
43	114.7/107	–	–
47	105.8/107	–	–

NOTES: The probability that a source is variable in either observation, according to the χ^2 and K-S tests. We only quote probabilities greater than 95 per cent so as to highlight possible variability.

in the spectral fitting in each case. The spectral analysis was performed using the spectral fitting package XSPEC (v.11.3.0). Spectral channels were grouped so as to give a minimum of 20 counts per bin, thus ensuring χ^2 statistics are valid. The pn, MOS-1 and MOS-2 spectra from both observations were fitted simultaneously, but we included constant multiplicative factors in each model to allow for calibration differences between the cameras. This value was frozen at unity for the pn data and allowed to vary for the MOS detectors, with the values typically agreeing within 15 per cent.

Initial fits to the X-ray spectra of the three bright sources, most likely associated with NGC 55 (*i.e.*, 20, 43, 47), were made using single component models in XSPEC. These included power-law (PO), blackbody (BB), multi-colour disc blackbody (DISKBB: an approximation of the optically-thick thermal X-ray spectrum of an accretion disc [Mitsuda et al. 1984, Makishima et al. 1986]),

Table 4. Matches of the *XMM-Newton* sources with sources in other catalogues.

<i>XMM</i> ID	<i>ROSAT</i> ID PSPC	HRI	Other ID	Source type
8			APM B001129.07-391943.0	Galaxy
17	N55-1			
20*	R1,S19, N55-2	N55-2		
27*	N55-3			
29	S18			
35*			BS2000-17	Galaxy
38*	R2,S17, N55-4	N55-4		
39	S16, N55-5	N55-5	UY Scl	Variable Star
41	N55-6	N55-6		
42	S14, RXJ 001451.5-392417			
43*	R3, S15,N55-7	N55-7		
46	1WGA J0014.9-3916, N55-8			
47*	R4, S13	N55-9		
48*			HDW86 - RS	Radio Source
52*	R5, S11, N55-10		HDW86 - RS	Radio Source
55*	N55-11			
58*			HK83-08, HDW86 - RS	HII region, Radio Source
71*	R6,S7, N55-14	N55-14	XMMU J001528.9-391319	ULX, XRB
72			LCRS B001300.1-392355	Galaxy
74*	R7, N55-15			
77			LCRS B001306.8-392624	Galaxy
79*	N55-16			
81	1WGA J0015.6-3926			
84*	N55-17			
87	N55-18			
90	N55-19		LA43	Globular cluster
94			APM B001321.45-391912.8	Galaxy
101*	N55-20			
110	N55-22			
112*	N55-23			
117*	N55-24			
118	1WGA J0016.1-3920, N55-25			
122*			LCRS B001349.4-393325	Galaxy
123			APM B001352.34-394040.4	Galaxy
125	1WGA J0016.5-3905			
132			LCRS B001412.2-393501	Galaxy
137	1WGA J0017.0-3910			

NOTES: *ROSAT* ID numbers refer to Read et al. (1997) (R#), Schlegel et al. (1997) (S#) and Roberts (1997) (N55-#). Other references: APM - Maddox et al. (1990); 1WGA - White, Giommi, & Angelini (2000), BS2000 - Beasley & Sharples (2000); UY Scl - Perryman et al. (1997); RXJ - Barber, Roberts, & Warwick (1996); HK83- Hodge & Kennicutt (1983); HDW86 - Hummel et al. (1986) (*i.e.*, the triple radio source); XMMU - Stobbart et al. (2004); LCRS - Shectman et al. (1996); LA43 - Liller & Alcaïno (1983).

bremsstrahlung (BREMSS) and solar-abundance optically-thin thermal plasma (MEKAL) spectral forms. An intervening absorption column (TBABS, utilising the relative interstellar abundances and absorption cross-sections tabulated by Wilms et al. 2000) was applied in each case. Typically, the best fits were obtained with either the PO or the DISKBB models. These results are summarised in Table 6, which also lists the observed 0.3 – 10 keV fluxes and the observed and intrinsic (unabsorbed) luminosities for the best fitting model. The spectra of sources 20 and 47 are best described by a simple absorbed power-law continuum with $\Gamma \sim 1.7$ and 1.8 respectively, although in both cases the DISKBB model also provides a statistically acceptable fit (with $kT_{in} \sim 1.7$ and 1.5 keV respectively). However, a power-law model is rejected (at > 99.99 per cent probability) for source 43, which is instead very well fitted by a DISKBB model with an inner disc temperature of ~ 0.8 keV. We note that a marginally better fit for source 43 was achieved using an absorbed bremsstrahlung model (with parameter values

$kT \sim 1.9$ keV, $N_H \sim 2.4 \times 10^{21} \text{ cm}^{-2}$ and χ^2/dof of 546.5/573). Fig. 5 shows the spectra and best fitting single component model in each case.

Given the high apparent X-ray luminosities of these sources, *i.e.*, close to or exceeding the Eddington limit for spherical accretion on to a $\sim 1.4 M_{\odot}$ neutron star, we also attempted to fit the data with the canonical model for black hole X-ray binary spectra, namely a combination of DISKBB and PO components (subject to absorption). This two component model provided an improvement to the spectral fits for all three sources, albeit with varying degrees of improvement ($\Delta\chi^2 \sim 4.5 - 44$ for two extra degrees of freedom).

The resulting inner-disc temperatures for sources 20 and 47 are unusually low for ‘normal’ luminous stellar-mass black hole binaries ($kT_{in} \sim 0.7 - 2$ keV, *cf.* McClintock & Remillard 2003), hence we also tried alternative (BB, MEKAL) models for the soft component. These produced equally good fits to the data, although

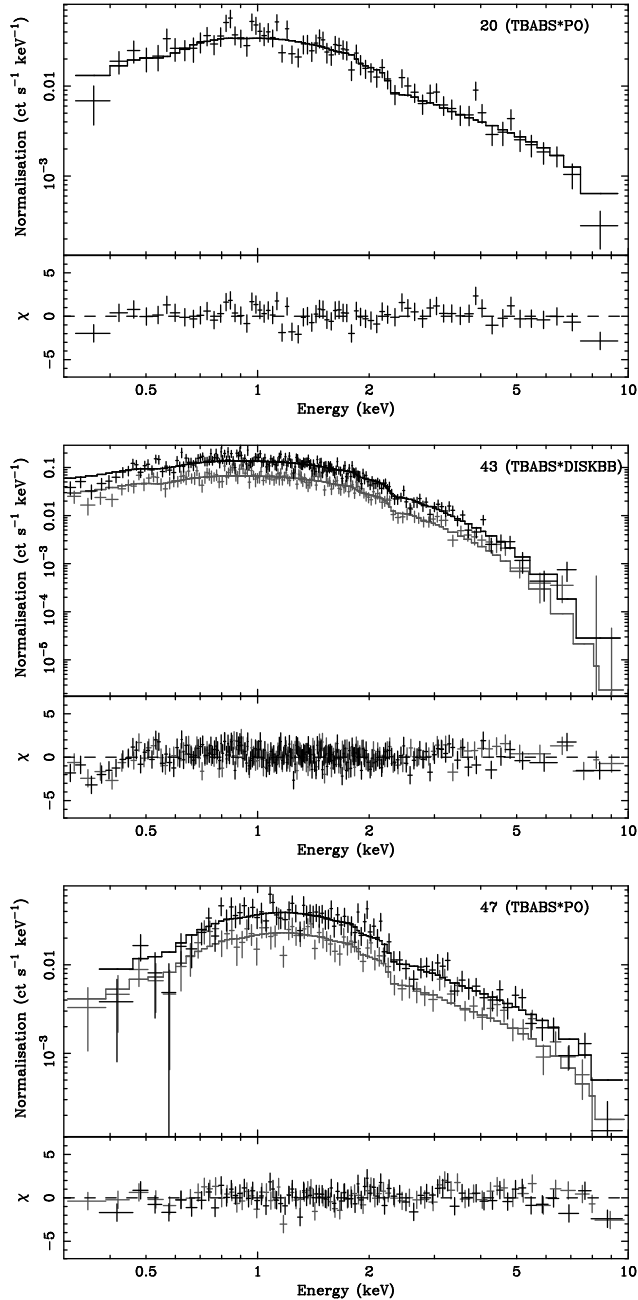


Figure 5. EPIC pn count rate spectra and $\Delta\chi$ residuals with respect to the best-fitting single component model specified in Table 6, for sources 20, 43 and 47. Data from the first and second observations are shown as grey and black respectively.

we note that in all cases the soft components only account for a small fraction (~ 6 per cent) of the total observed X-ray flux. In the case of the fits to source 43, we obtained an even more puzzling result; the power-law fitted to the soft end of the X-ray spectrum. Similar results have been seen for several ultraluminous X-ray sources, including source 71 in the same host galaxy (e.g. Stobbart et al. 2004; Roberts et al. 2005), where the presence of such a power-law component is difficult to explain physically, and as such the power-law is most likely a proxy for another soft component. We therefore attempted both the alternative model fits as

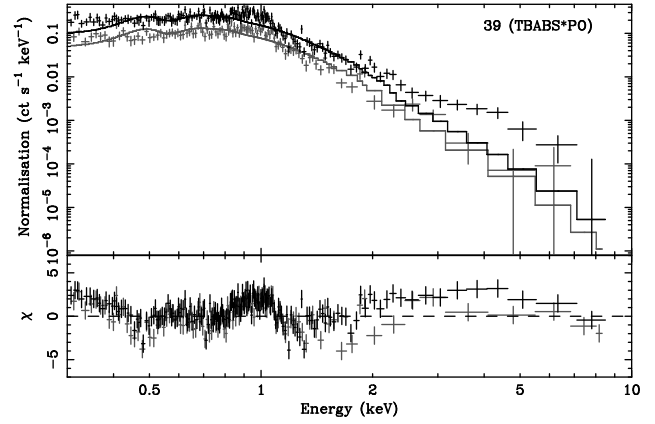


Figure 6. EPIC pn count rate spectra and $\Delta\chi$ residuals for a simple power-law continuum model fit to source 39 (the putative foreground star). The data are displayed as in Fig. 5.

per sources 20 and 47, that also resulted in improved fits to source 43.

We quantify the statistical significance of the improvement offered by these additional components (above the simple single component fits) using the prescription described in sec. 5.2 of Protassov et al. (2002)⁴. This uses a Monte Carlo recipe for XSPEC to simulate the expected reference distribution of F-values based on an input power-law spectrum. This reference distribution yields a confidence probability for the fit improvement, as shown in Table 7. Our simulations show that the two-component modelling provided significant improvements ($\gtrsim 3\sigma$, at the best resolution of our simulations) over a simple power-law model for source 47, and over a DISKBB for source 43. However, the $\Delta\chi^2 \sim 5$ improvements for source 20, for two extra degrees of freedom, were not significant (at a probability of < 90 per cent), hence we do not show these fits in Table 7. We discuss the plausibility of these spectral solutions in sec. 7.

Fig. 6 shows that the final source (39), does not have a spectrum with a simple continuum shape. As this source is coincident with the $m_v = 11.5$ variable foreground star UY Scl and is presumably a stellar coronal source, we first attempted to fit its X-ray spectrum with a thermal plasma (MEKAL) model. However, a single temperature MEKAL model resulted in an unacceptable fit, with a reduced χ^2 (i.e. χ^2_ν) ~ 1.7 , even after allowing its abundance to vary from solar. This was due, in part, to an apparent increase in the hardness of the source at energies > 2 keV in the second observation (*cf.* Fig. 6). We attempted to model this by allowing the MEKAL component temperature and normalisation to vary between the two observations, but this approach proved unsuccessful. However, the addition of a second, hotter MEKAL component, with a normalisation free to vary between the observations did lead to a significant improvement in the fit ($\chi^2_\nu \sim 1.2$), although residuals remained evident above 2 keV. An acceptable fit was finally produced by the addition of a third MEKAL component, and again allowing the normalisation of the hottest MEKAL to vary between the observations (whilst keeping the others constant, and constraining them to the same abundance). We detail the best fit in Table 8. The variation in the hottest component was considerable, implying at least a factor

⁴ The F-test **should not** be used in the case of additive model components, because it does not follow its expected theoretical reference distribution in this case (Protassov et al. 2002).

10 increase in its strength between the two observations, although even at its brightest level (in the second observation) its contribution to the total 0.3 - 10 keV source flux amounts to only ~ 20 per cent.

The low absorption column (set at Galactic) and multi-temperature thermal plasma spectrum provide strong support for the origin of the X-ray emission to be in the stellar corona of an active star in our own Galaxy. Temperatures of ~ 0.3 and 1 keV are typical for such objects, however a prominent emission component at temperatures at or above 2 keV is commonly seen only in young stars or active binaries (such as RS CVns), and rarely in main sequence stars except during flares (Güdel 2004). A published optical spectrum reveals radial velocity variations of $\sim 40 \text{ km s}^{-1}$ (Solano et al. 1997), characteristic of a close binary star system, and the 2MASS colours of UY Scl reveal it to have a late (possibly K-giant) spectral type. Therefore, a plausible interpretation of the X-ray and optical properties of the variable star UY Scl is that it is a previously-unidentified RS CVn system.

5 X-RAY COLOURS

X-ray colour classification has recently been used by Prestwich et al. (2003) and Kilgard et al. (2005) to provide a statistical distinction between populations of X-ray binaries (XRBs) and supernova remnants (SNRs) observed in nearby galaxies. This scheme, which was originally applied to *Chandra* observations, is useful when the X-ray data are too limited for detailed spectral diagnostics to be considered on a source by source basis. In this work, we use an adaptation of this X-ray colour classification scheme tuned to *XMM-Newton* data (Jenkins et al. 2005)⁵.

The basic approach is to divide the HR1 versus HR2 colour space into sub-regions so as to distinguish different classes of X-ray source, albeit within the limits set by the overlapping spread of spectral form which characterises the various populations. The measurement uncertainties on the X-ray colours (HR1 and HR2) also serve to blur the population boundaries. Here we divide the set of sources detected within the D_{25} ellipse of NGC 55 into four broad categories of source: ‘absorbed’, ‘XRB’, ‘SNR’ and ‘other’ sources using the same criteria as employed by Jenkins et al. (2005) in their study of M101⁶. In the event, there were no sources in NGC 55 falling in the ‘other’ category and, for our current purpose, we have combined the ‘absorbed’ and ‘XRB’ sources into a single ‘XRB’ category.

However, we have also added a further sub-division of the soft X-ray source population using the criterion, $\text{HR1} < -0.8$, to classify sources as ‘very soft’ sources (VSSs)⁷. This class could contain a menagerie of exotic sources, including true supersoft sources (SSSs). SSSs emit X-rays predominantly below 0.5 keV (Greiner 2000). Most are believed to be accreting white dwarfs undergoing nuclear burning on their surface (van den Heuvel et al. 1992; Rappaport, Di Stefano, & Smith 1994).

Other possibilities for very soft emitters include some SNRs, accreting neutron stars with large photospheres, intermediate-mass black holes, symbiotic systems, the hot cores of young planetary nebulae and stripped cores of tidally disrupted stars (e.g., Di Stefano & Kong 2004). Our classification will also contain those sources classed as ‘quasi-soft’ by Di Stefano & Kong (2004), which could include slightly hotter and/or absorbed variants on the above source types.

However, while our chosen energy bands provide good signal to noise coverage for the data in general, extra soft energy sub-bands are required for more confident identifications of true SSSs. This has been explicitly demonstrated for *XMM-Newton* data from the galaxies M33 (Pietsch et al. 2004) and M31 (Pietsch et al. 2005a) and the emission of optical novae within them (Pietsch et al. 2005b). We therefore extracted 0.3 - 0.5 keV images from each dataset, and performed aperture photometry at the positions of the VSSs. On the basis of this, we were able to identify sources 53 and 63 as good candidate SSSs due to the vast majority of their detected source counts originating below 0.5 keV. The remaining 5 VSSs were all dominated by 0.5 - 1 keV counts.

On the basis of this X-ray colour classification scheme there are 30 XRBs, 5 SNRs and 7 VSSs within the D_{25} ellipse of NGC 55. Earlier we concluded that 10-15 of the sources within D_{25} ellipse might in fact be background sources (largely AGN) seen through the disc of the galaxy. Since the absorption in the disc of NGC 55 will preferentially suppress the soft emission of background objects, we would expect such background sources to reside predominantly in the XRB (and ‘absorbed’ source) colour range. Background objects could therefore account for between 30 per cent - 50 per cent of the sources in the XRB category. The ratio of ‘hard’ XRBs to ‘soft’ sources (SNRs, VSSs and ‘other’ sources) observed in NGC 55 (roughly 60 per cent:40 per cent) is very similar to that seen in M101 (Jenkins et al. 2005), after (in both cases) applying a rough correction for background source contamination. Since these are respectively edge-on and face-on systems, one might conclude that to zeroth order the inclination of a galaxy does not impact the relative prominence of the hard and soft X-ray source populations. Of course in practice, factors such as the radial distribution and scale height of the various populations and the depth of the absorption associated with the galactic disc, combine to make this a complex problem.

Perhaps one surprising result of this analysis is that VSSs make up one sixth of the total source population detected within the D_{25} ellipse of NGC 55, and could constitute more than one in four sources after the exclusion of background contamination. We have investigated whether this is an unusually large fraction by comparison to published *XMM-Newton* and *Chandra* studies that detect VSSs in other nearby galaxies. Firstly, we note that only ~ 12 per cent of the D_{25} sources of M101 in an *XMM-Newton* observation are classified as VSSs using our criterion (c.f. Jenkins et al. 2005). As a wider comparison, we also looked at the VSS population of M101 in a much deeper *Chandra* (ACIS-S) observation, as well as those of M83 (face-on spiral), M51 (interacting galaxy) and NGC 4697 (elliptical) (Di Stefano & Kong 2004). We converted our *XMM-Newton* HR1 VSS criterion to the equivalent *Chandra* ACIS-S value (via WEBPIMMS), using the appropriate energy bands, to facilitate comparison. Using only our criterion, we found that the fraction of VSSs were 31 per cent for M101, 25 per cent for M83, 15 per cent for M51 and 4 per cent for NGC 4697. At first glance, it therefore appears that there are quite large variations in the VSS population fractions of different galaxies. However, this fraction could be extremely susceptible to observational effects

⁵ An alternative classification scheme developed specifically for *XMM-Newton* data is described in Pietsch et al. (2004).

⁶ Here ‘other’ sources refers to the background and indeterminate soft/hard source categories in Table 3 of Jenkins et al. (2005).

⁷ This definition is similar, although not identical, to the definition of very soft sources used by Di Stefano & Kong (2003). For example, they base their work on *Chandra* ACIS-S data, use slightly different bands and have additional selection criteria.

Table 6. Spectral fitting of single component models for three bright sources in NGC 55

Source	PO ^a			DISKBB ^a			f_X^b Obs	L_X^c	
	N_H^d	Γ	χ^2/dof	N_H^d	kT_{in}	χ^2/dof		Obs	Unabs
20	2.56 ^{+0.44} _{-0.39}	1.67 ^{+0.09} _{-0.08}	125.6/119	0.80 ^{+0.26} _{-0.24}	1.65 ^{+0.14} _{-0.12}	130.9/119	3.52 ^{+0.23} _{-0.27}	1.33 ^{+0.09} _{-0.10}	1.67 ^{+0.08} _{-0.15}
43	4.23 \pm 0.20	2.70 \pm 0.05	715.0/573	1.25 \pm 0.11	0.79 \pm 0.02	551.3/573	6.33 ^{+0.11} _{-0.14}	2.40 ^{+0.04} _{-0.09}	2.90 ^{+0.03} _{-0.09}
47	4.64 ^{+0.47} _{-0.44}	1.84 \pm 0.07	252.0/276	2.05 ^{+0.28} _{-0.26}	1.50 ^{+0.09} _{-0.08}	278.2/276	4.60 ^{+0.20} _{-0.24}	1.74 ^{+0.08} _{-0.09}	2.55 ^{+0.05} _{-0.19}

NOTES: ^a Spectral models are abbreviated to XSPEC syntax: PO – power-law continuum; DISKBB – multicolour disc black body emission; ^b Observed 0.3–10 keV X-ray flux ($\times 10^{-13}$ erg cm⁻² s⁻¹); ^c Observed and intrinsic 0.3–10 keV X-ray luminosity ($\times 10^{38}$ erg s⁻¹); ^d Column density (including Galactic, $\times 10^{21}$ cm⁻²). The best fitting model for each source is highlighted by showing the χ^2/dof values in bold face.

Table 7. Two-component spectral modelling results

Source	Model ^a	N_H	$\Gamma/kT/kT_{in}^b$	kT_{in}/Γ^c	χ^2/dof	$\Delta\chi^2^d$	f_X fraction ^e	
							Soft	PO
43	PO+DISKBB	5.62 \pm 0.11	4.91 ^{+0.74} _{-0.78}	0.82 \pm 0.04	507.3/571	44.0	0.27	0.73
	BB+DISKBB	2.57 ^{+0.86} _{-0.42}	0.14 \pm 0.02	0.81 ^{+0.03} _{-0.04}	513.5/571	37.8	0.1	0.9
	MEKAL+DISKBB	1.67 ^{+0.25} _{-0.21}	0.28 ^{+0.06} _{-0.04}	0.80 \pm 0.02	522.9/571	28.4	0.04	0.96
47	DISKBB+PO	10.97 ^{+1.56} _{-2.23}	0.11 ^{+0.02} _{-0.01}	2.08 ^{+0.09} _{-0.13}	234.1/274	17.9	0.06	0.94
	BB+PO	10.41 ^{+2.36} _{-2.21}	0.10 \pm 0.01	2.06 ^{+0.11} _{-0.12}	234.1/274	17.9	0.06	0.94
	MEKAL+PO	9.33 ^{+2.39} _{-2.52}	0.24 ^{+0.09} _{-0.05}	1.99 ^{+0.12} _{-0.14}	234.3/274	17.7	0.06	0.94

NOTES: ^a Spectral models are abbreviated to XSPEC syntax: PO and DISKBB as before, BB - blackbody continuum, MEKAL - solar-abundance thermal plasma model. The dominant soft component is listed first. ^b Value of characteristic parameter for soft component. ^c Value of characteristic parameter for hard component. ^d χ^2 improvement over the best-fitting single component fit, for two extra degrees of freedom. ^e Fraction of the total observed flux in the soft and power-law components. The significance probability of the fit improvement over the single component fit is 100 per cent in each case, based on the resolution of the Monte Carlo simulations described in the text (200 simulations per source).

Table 8. Three-temperature MEKAL spectral model for UY Scl.

Parameter	Value
N_H ($\times 10^{21}$ cm ⁻²)	0.155 (<i>fixed</i>)
kT_1 (keV)	0.33 \pm 0.02
kT_2 (keV)	1.00 \pm 0.04
kT_3 (keV)	3.44 ^{+2.39} _{-1.27}
Abundance (solar units)	0.43 ^{+0.08} _{-0.07}
χ^2/dof	512.6/463

such as the effective (foreground and intrinsic) extinction and the luminosity threshold of the observations. For example, as typical SSSs in particular have luminosities below $\sim 10^{37}$ erg s⁻¹, this latter effect should result in more SSSs being observed in deeper, more sensitive observations, as may be the case when comparing the deep *Chandra* observation of M101 with the shallower *XMM-Newton* data. The Galactic foreground absorption is certainly a very important factor on the number of VSSs detected – this is small in M101, M83 and NGC 55 but is significantly higher in M51 and NGC 4697. An additional influence on the number of VSSs detected is the choice of filter used in the observations. The *XMM-Newton* observations of M101 were made using the medium filter while the NGC 55 observations utilised the thin filter. We conclude that although the differences between galaxies appear large, selection effects may dominate.

6 RESIDUAL DISC EMISSION

The individual *XMM-Newton* observations were flat-fielded by subtracting a constant particle rate from the image (estimated by taking an average of the count rates in the edge regions of the detector not exposed to the sky) and then dividing by the appropriate exposure map. In the same process, bad pixels, a hot column (for the pn detector) and spurious data along chip gaps were excised. The flat-fielded data from the two observations were then mosaiced into a single exposure-corrected image. Here we focus our attention on the pn soft-band data.

Fig. 7 shows the mosaiced pn soft-band image of the central region of the galaxy. In order to highlight unresolved or possible diffuse emission (which we refer to hereafter as the residual disc emission), we have blanked out regions around the catalogued discrete sources listed in Table 2. For this purpose, circular exclusion regions were used of radius 20'', 40'', 1' or 2' depending on the strength of the source⁸. An exception was made for sources 48, 52 and 58, which have X-ray colours characteristic of SNRs and which we here consider as part of the diffuse component of the galaxy. The residual emission is concentrated in the central disc of NGC 55 encompassing both the bar region and the region to the immediate east of the bar. The presence of several relatively bright X-ray

⁸ These sizes were determined empirically based on the need to suppress high levels of contamination from point sources, consistent with the size and shape of the point-spread function over the wide range of offset angles sampled.

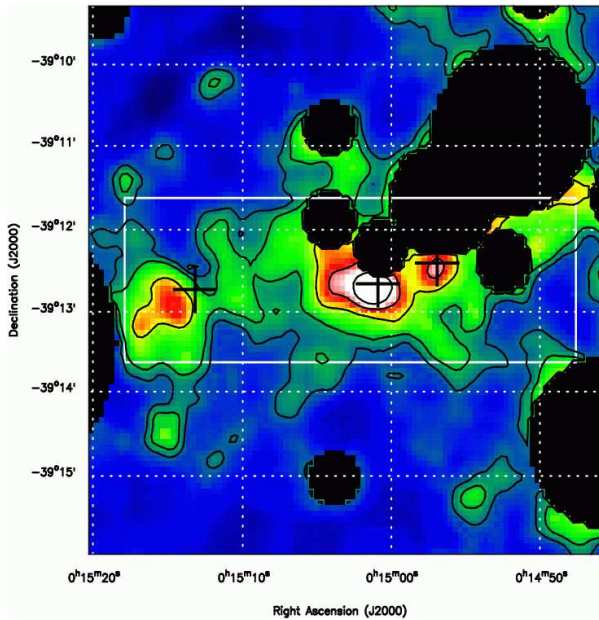


Figure 7. Close up of the composite flat-fielded pn image in the soft (0.3–1.0 keV) bandpass. Regions around catalogued sources have been blanked out so as to reduce the contamination of the diffuse signal by relatively bright resolved point sources. An exception was made for three sources in the region (sources 48, 52 and 58) whose positions are indicated by crosses, which have HR1 values characteristic of SNRs (see text). The large rectangle, excluding the blanked out sections, corresponds to the region used to estimate the diffuse luminosity of the disc of NGC 55 and from which the diffuse spectrum was extracted.

sources makes it difficult to delineate the full extent of this component along the disc, although on the basis of Fig. 3 it appears to be $\lesssim 12'$. The residual emission is most evident within $\pm 1'$ of the plane, which is well within the extent of the thin disc component (Davidge 2005).

We estimate the *observed* (0.3–1 keV) luminosity of the disc within the $6' \times 2'$ rectangular region illustrated in Fig. 7 (excluding the blanked out regions) to be 2.5×10^{37} erg s $^{-1}$ (based on the observed count rate in this band, and energy conversion factors derived from the spectral analysis discussed below). Several regions of enhanced surface brightness are evident within this region, two of which are clearly related to sources 48 and 52. The easternmost bright region appears to be offset from source 58 but we note that this source was detected at relatively low significance only in the MOS soft band channel. Judging from the pn soft band image, the position of peak X-ray surface brightness is located approximately 1 s (of time) east of the catalogued position of source 58⁹. The three X-ray bright regions identified above, all coincide with radio sources and, in fact, X-ray sources 52 and 48 correspond to the core and eastern component of the triple source identified by Hummel et al. (1986). These regions are also prominent in H α (Ferguson et al. 1996) and in the *Spitzer* far-infrared (24 μ m) image of NGC 55 (Engelbracht et al. 2004) and correspond to sites of current star formation in the disc of NGC 55. Together the three bright regions contribute roughly 30 per cent of the inferred residual disc X-ray luminosity.

⁹ The fact that this region was not detected as a discrete source in the pn data may reflect a limitation in the background modelling in the vicinity of the brightest X-ray source in NGC 55.

We have extracted spectra representative of the residual disc emission of NGC 55 from the rectangular region shown in Fig. 7 (excluding the blanked out regions) using a background spectrum obtained from a nearby region of the same dimension (from which catalogued sources were also excluded). The diffuse spectra were grouped to give a minimum of 30 counts per bin. The six available spectral datasets (pn, MOS-1 and MOS-2 data from two observations) were fitted simultaneously, but with the relative normalisations untied so as to allow for calibration differences between the cameras. The spectral analysis was confined to the 0.3–6 keV energy range for which there was a reasonable signal to noise ratio.

Initially, we modelled the X-ray spectra with an absorbed MEKAL component, with the abundance free to vary. This yielded $N_H \sim 2 \times 10^{21}$ cm $^{-2}$ and $kT \sim 0.5$ keV, with a very low inferred abundance of $Z \sim 0.04 Z_\odot$ ($\chi^2/\text{dof}=307/217$). An improved fit to the data was achieved with the inclusion of an additional harder spectral component, either in the form of a power-law or higher temperature MEKAL emission. Table 9 details the best-fit parameters for these two-component models. The observed pn spectra and the best-fitting MEKAL plus power-law model is shown in Fig 8.

The derived flux using the MEKAL plus power-law model is $\sim 1.6 \times 10^{-13}$ erg cm $^{-2}$ s $^{-1}$ (0.3–6 keV), corresponding to an absorbed luminosity of 6×10^{37} erg s $^{-1}$. Roughly half of this luminosity is contributed by the soft thermal emission.

The measured column density of 5.1×10^{21} cm $^{-2}$ is much greater than the foreground column in our own Galaxy, and is consistent with the location of this residual component within the central disc region of NGC 55. If we correct for this absorption the inferred luminosity of the soft component increases to $\sim 3 \times 10^{38}$ erg s $^{-1}$. A reasonable hypothesis is that the soft emission represents a truly diffuse component energised by processes linked to regions of recent star formation (collision of stellar winds in dense environments, supernovae and shock heating in SNRs), whereas the harder spectral component (most appropriately modelled as a power-law) arises largely in unresolved XRBs.

The derived temperature of the soft residual disc emission in NGC 55 is ~ 0.2 keV (Table 9). This is fairly typical of the softest emission seen in more luminous star-forming galaxies where the temperature range for diffuse disc components may extend up to ~ 2 keV (e.g., Pietsch et al. 2001, Fabbiano et al. 2003). By analogy to these systems, it is very likely that the hot diffuse gas in NGC 55 is, in fact, a multi-temperature medium. The very low abundance derived for this hot gas component (Table 9) is almost certainly an artefact of fitting a complex spectrum with a very simplified model.

On the one hand the above determination of the luminosity of the residual disc component in NGC 55 represents only a lower limit estimate given that we have not measured the true extent of the disc component and, even within the inner $6' \times 2'$ region (corresponding to 3 kpc \times 1 kpc at the distant of NGC 55) we have of necessity excluded regions around bright sources. On the other hand the *observed* X-ray flux of the residual disc emission is only ~ 3 per cent of that of the resolved sources in the broad 0.3–6 keV band or a 6 per cent fraction if we consider only the soft band. Since the point spread function of the *XMM-Newton* optics has wings extending well beyond the blanked-out regions in Fig. 7, some contamination of the residual disc component by the nearby bright sources is inevitable. However, since the morphology of the extended emission (in Fig. 7) does not closely track the distribution of the bright sources, we can be confident that the residual signal (net of the local background) is not dominated by such contamination, at least in the soft band. Unfortunately the surface brightness

Table 9. Spectral modelling results for the residual disc emission

Model	N_H^a	kT_1^b	kT_2^b	$Z (Z_\odot)^c$	Γ	χ^2/dof	f_X^d		
							Obs	Obs	Unabs
MEKAL	$2.0^{+0.4}_{-0.6}$	$0.52^{+0.09}_{-0.05}$	–	0.04 ± 0.02	–	307/217	0.94	0.36	0.83
MEKAL+PO	$5.1^{+1.8}_{-2.0}$	$0.21^{+0.01}_{-0.03}$	–	$0.07^{+0.07}_{-0.03}$	$1.9^{+0.4}_{-0.3}$	230/215	1.55	0.59	3.87
MEKAL+MEKAL	$5.3^{+0.9}_{-2.0}$	$0.20^{+0.06}_{-0.04}$	$4.52^{+9.19}_{-2.12}$	$0.06^{+0.10}_{-0.03}$	–	231/215	1.44	0.55	4.52

NOTES: ^a Column density (including Galactic, $\times 10^{21} \text{ cm}^{-2}$). ^b Temperatures of the cool (kT_1) and hot (kT_2) thermal components in keV. ^c Relative metal abundance of the thermal plasma component. ^d Observed 0.3–6 keV X-ray flux ($\times 10^{-13} \text{ erg cm}^{-2} \text{ s}^{-1}$). ^e Observed and intrinsic (absorption-corrected) 0.3–6 keV X-ray luminosity ($\times 10^{38} \text{ erg s}^{-1}$).

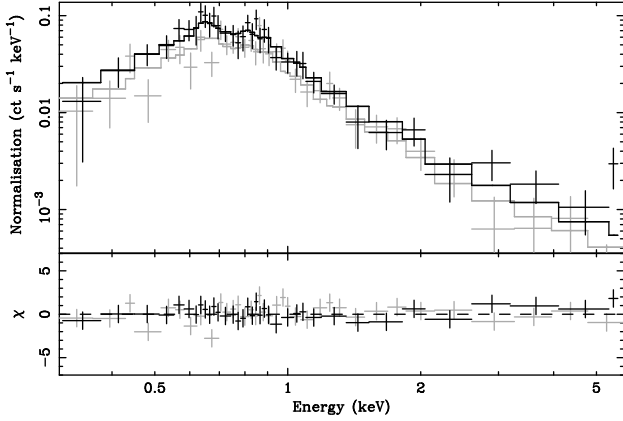


Figure 8. EPIC pn count rate spectra for the residual disc emission in NGC 55 from the first (grey) and second (black) observations. The best-fit MEKAL plus power-law model is shown along with the corresponding $\Delta\chi$ residuals (lower panel). NB The data have been rebinned for illustrative purposes using SETPLOT REBIN in XSPEC

of the residual emission is too low to apply a similar imaging test above 1 keV.

Using the parameters from the MEKAL plus power-law model, we have derived the physical properties of the soft residual disc component as summarised in Table 10 (this Table includes a description of the parameters of the diffuse emission introduced below). Similar values have been obtained by Summers et al. (2003) for the cool diffuse disc component seen in the Magellanic irregular NGC 4449. These authors note that the diffuse medium is likely to be clumpy with a filling factor $f < 1$, implying that the quoted values for n_e and P are underestimates, whereas M , E_{th} and t_{cool} are overestimated. The derived pressure of the hot gas in NGC 55, $P/k \sim 1.5 \times 10^5 \text{ K cm}^{-3}$, which is similar to the pressure inferred for the interior of the Loop 1 superbubble within our own Galaxy (Willingale et al. 2003). This is broadly consistent with the view that there has been sufficient recent star formation in the disc of this low-mass dwarf system to form expanding hot bubbles, which result in the ejection of material out of the disc of the galaxy into the halo. However, the absence of an extended extra-planar soft X-ray component in NGC 55 (contrary to the findings of Oshima et al. 2002) suggests that the gas in such bubbles cools relatively quickly through adiabatic losses (given the relatively long radiative cooling timescale in Table 10), retaining insufficient energy to power a superwind of the form frequently seen in systems with star-formation rates, $\text{SFR} > 1 M_\odot \text{ yr}^{-1}$ (Strickland 2004).

Table 10. Physical parameters of the soft residual disc component.

Physical property	Value
Temperature, T	$2.4 \times 10^6 \text{ K}$
Intrinsic L_X	$3.3 \times 10^{38} \text{ erg s}^{-1}$
Electron density, n_e	0.029 cm^{-3}
Thermal energy, E_{th}	$6.8 \times 10^{54} \text{ erg}$
Mass of hot gas, M	$5.7 \times 10^6 M_\odot$
Pressure, P	$2.0 \times 10^{-11} \text{ dyn cm}^{-3}$
Cooling time, t_{cool}	$6.5 \times 10^8 \text{ yr}$

ASSUMPTIONS: $V = 2 \times 10^{65} \text{ cm}^3$ (cylindrical volume subtending $6' \times 2'$ on the sky); $D = 1.78 \text{ Mpc}$; filling factor, $f = 1$; $n_e = (EI/Vf)^{1/2}$, where EI is the emission integral ($norm \times 4\pi D^2$)/ 10^{-14} , and $norm$ is the MEKAL normalisation obtained from the spectral fitting; $E_{th} = 3n_e kTV$; $M = n_e m_P V f$; $P = 2n_e kT$ and $t_{cool} \sim (3kT)/(\Lambda n_e)$, where $\Lambda = L_X/EI$.

7 DISCUSSION

7.1 The brightest sources in NGC 55

What is the nature of the luminous X-ray source population observed in NGC 55? This question is most easily addressed for the brightest subset of X-ray sources, wherein the information provided by X-ray diagnostics is at its richest. The brightest X-ray source in NGC 55 (XMMU J001528.8-391318, source 71) has an X-ray luminosity $L_X \sim 10^{39} \text{ erg s}^{-1}$ placing it on the boundary of the ULX classification. As discussed in Paper I this source is a candidate luminous black hole X-ray binary. In sec. 4 we reported the details of four out of the five next brightest X-ray sources in the NGC 55 field. One of these sources (39) is spatially coincident with a bright variable foreground star at the edge of the D₂₅ ellipse, and its X-ray properties suggest that it may be a previously unidentified RS CVn system. Of the other three sources, two are located in the bar region and one in the western limb of the NGC 55 disc. A combination of their high luminosities ($L_X > 10^{38} \text{ erg s}^{-1}$), measured absorption columns far in excess of the Galactic foreground, and power-law continuum or accretion disc dominated X-ray spectral shapes (see sec. 4.2), argues that these sources are likely to be X-ray binaries in NGC 55, though a clearer detection of short-term variability is required to confirm this. Indeed, since the apparent high intrinsic X-ray luminosities of these sources are close to or in excess of the Eddington limit for a 1.4- M_\odot neutron star, the primary accreting object in these systems may be a black hole. This hypothesis is supported by the X-ray spectroscopy. We would expect a bright neutron star X-ray binary spectrum to be described by a combination of a $\sim 1.5 \text{ keV}$ accretion disc and a $\sim 2 \text{ keV}$ blackbody spectral component with the latter originating in the

neutron star envelope (*c.f.* Jenkins et al. 2004). Instead our X-ray spectra appear to be more typical of ‘low’ (hard power-law dominated) and ‘high’ (thermal accretion disc dominated) black hole spectral states (*cf.* McClintock & Remillard 2003). The long-term (~ 9 year) persistence of these sources, and their locations close to the star-forming regions in the disc of NGC 55, suggest that these may be systems containing a high-mass secondary star.

One interesting result from the spectral analysis of sources 43 and 47 is the detection of a very soft component in each spectrum (a similar component is seen in source 20, but does not provide a statistically robust improvement to the fit). The temperature of this component in source 47, when modelled by a DISKBB, is ~ 0.1 keV. This is remarkably similar to the $\sim 0.1 - 0.3$ keV temperatures derived for the very soft components seen in some nearby ULXs which, it has been argued, may be evidence for the presence of a $\sim 1000 M_{\odot}$ ‘intermediate-mass’ black hole (IMBH) (e.g. Miller et al. 2003). So should we interpret the soft spectra of this source (which is one to two orders of magnitude less luminous than ULXs) in the same way? If ULXs are accreting IMBHs, then one might expect to see a range of accretion rates, and hence luminosities, across the population, as is commonly the case for Galactic black hole binaries. However, on this basis one might predict a change in the spectrum to a ‘low’ state as the luminosity decreases, whereas the spectra for the NGC 55 sources appear very similar to the apparent ‘high state’ spectrum of IMBH candidates (though in these cases, as in some ULXs, the power-law slope is anomalously hard for a true high state; see Roberts et al. 2005). The overall spectral shape ($\Gamma \sim 2$ power-law, $kT_{in} \sim 0.1$ keV DISKBB) might actually also describe the ‘low’ state for an ordinary black hole X-ray binary, which (at a luminosity of $\sim 1 - 2 \times 10^{38}$ erg s $^{-1}$) must be a plausible alternative for this source.

The shape of the spectrum of source 43 potentially mirrors another result to emerge from recent ULX studies, an X-ray spectrum described by a hot $0.7 - 2$ keV DISKBB with a very soft power-law dominant at low energies. The physical implausibility of this spectral description is discussed by various authors, who note alternative empirical solutions (e.g. replacing the power-law with a blackbody emission spectrum) or physical models (e.g. optically-thick Comptonisation) that can explain the spectrum (see Feng & Kaaret 2005, Stobbart, Roberts, & Wilms 2006).

However, a more mundane alternative for the nature of the soft emission in both sources is suggested by the fact that they are also well-fitted by a MEKAL component. The derived MEKAL temperature ($\sim 0.2 - 0.3$ keV in each case) is similar to the temperature of the residual emission detected in the galaxy. Also, the surface brightness required to produce the observed signal within the source extraction regions is within a factor of ~ 2 of the average surface brightness seen elsewhere in the NGC 55 disc (see sec. 6). It seems quite likely, therefore, that this very soft component is simply the underlying emission of the disc of NGC 55 contaminating the source signal¹⁰.

7.2 NGC 55 - a typical Magellanic-type galaxy

Although the near edge-on orientation has complicated efforts to study the morphology of NGC 55, the current consensus is that this galaxy is a dwarf irregular, structurally similar to the Large

¹⁰ We note that similar results are emerging in other *XMM-Newton* datasets, e.g., the soft excesses of ULXs in M51 are readily explained as local diffuse emission (Dewangan et al. 2005).

Table 11. The components of the integrated X-ray luminosity of NGC 55.

Component	L_X (0.3–6 keV)
Brightest (ULX) source	9.4×10^{38} erg s $^{-1}$
Next 20 brightest sources	6.9×10^{38} erg s $^{-1}$
VSSs	0.1×10^{38} erg s $^{-1}$
Residual soft disc ^a	3.3×10^{38} erg s $^{-1}$
Residual hard disc ^a	0.5×10^{38} erg s $^{-1}$

^a Corresponding to the $6' \times 2'$ inner disc region. Corrected for absorption intrinsic to NGC 55

Magellanic Cloud (LMC; see Davidge 2005). In order to address the question of whether NGC 55, from an X-ray perspective, is a typical Magellanic-type galaxy, we need to consider its overall X-ray properties. Earlier we concluded that there might be up to ~ 20 XRBs associated with NGC 55 in the sample of sources detected within its D_{25} ellipse, down to an effective luminosity threshold of 2×10^{36} erg s $^{-1}$ (0.3 – 6 keV). In addition, 7 VSSs were identified in the D_{25} sample. The integrated X-ray luminosity of these source categories together with the luminosity inferred for the residual disc emission (including SNRs) is summarised in Table 11. (Note that the discrete source luminosities are from Table 2 and are, in effect, observed luminosities, *i.e.*, uncorrected for absorption intrinsic to NGC 55.)

Other nearby examples of actively star-forming Magellanic-type systems include the LMC and NGC 4449, both of which have been extensively studied in X-rays (e.g., Wang et al. 1991; Vogler & Pietsch 1997; Bomans, Chu, & Hopp 1997; Sasaki et al. 2002; Summers et al. 2003). Table 12 compares the X-ray and other properties of these two galaxies with those of NGC 55 and illustrates the striking similarities of these systems. Total mass, mass in neutral hydrogen, star-formation rate (SFR) and the X-ray luminosity in discrete sources and diffuse components (more precisely the residual disc in the case of NGC 55) differ by no more than a factor of 3 across the three galaxies. All three systems would appear to follow the paradigm of strong spatial association of the bright X-ray emitters with the sites of current star-formation, with a scaling of X-ray luminosity to SFR broadly consistent with the L_X versus SFR correlation established for much more active systems (Ranalli et al. 2003; Gilfanov 2004).

8 SUMMARY

We have used recent *XMM-Newton* EPIC observations to investigate the X-ray properties of the Magellanic type galaxy NGC 55. A total of 137 X-ray sources were detected in the NGC 55 field of which 42 were located within the optical confines of the galaxy as defined by the D_{25} ellipse. The source detections cover a flux range of $\sim 5 \times 10^{-15} - 2 \times 10^{-12}$ erg cm $^{-2}$ s $^{-1}$ (0.3–6 keV) corresponding to a luminosity range of $\sim 3 \times 10^{35} - 9 \times 10^{38}$ erg s $^{-1}$ for sources at the distance of NGC 55. After allowing for some contamination of the sample by background AGN, our best estimate, based largely on X-ray colour classification, is that within the D_{25} region, we detect ~ 20 XRBs, 5 SNRs and 7 VSSs associated with NGC 55. Just outside the D_{25} ellipse, we also detected an X-ray source coincident with a globular cluster in NGC 55.

We have performed detailed X-ray spectral and timing analysis on four bright X-ray sources (> 500 counts) in the field of view (excluding the brightest source which was studied in Paper I). One

Table 12. A comparison of the properties of NGC 55 with those of two other Magellanic dwarf galaxies.

Property	LMC	NGC 55	NGC 4449
Assumed Distant (Mpc)	0.05	1.78	2.93
L_X (sources) ^a (10^{38} erg s ⁻¹)	5	17	14
L_X (diffuse) ^a (10^{38} erg s ⁻¹)	3	6	10
M_{25} ^b ($10^9 M_\odot$)	3.3	8.5	4.2
M_{HI} ^c ($10^9 M_\odot$)	0.6	2.0	1.6
SFR ^d (M_\odot yr ⁻¹)	0.25	0.22	0.2

NOTES:

^aX-ray luminosities from Wang et al. (1991); this paper; Summers et al. (2003) respectively

^b ‘Indicative’ mass of the galaxy within its D₂₅ diameter from Karachentsev et al. (2004).

^c HI mass of the galaxy from Karachentsev et al. (2004).

^d Star formation rates from Grimm et al. (2003); Thronson et al. (1987); Engelbracht et al. (2004) respectively.

Quoted values are scaled to the assumed distant.

of these objects is identified with a Galactic foreground star (UY Scl) and exhibits many of the properties of an RS CVn system. The other three are persistent X-ray sources with spectra indicative of accreting XRBs.

A residual emission component is also evident in the disc of NGC 55, concentrated on the bar region. The extent of this emission is at least 6' (3 kpc) along the plane of the galaxy and $\pm 1'$ (± 500 pc) perpendicular to the plane. We interpret the soft component as thermal diffuse emission with $kT \sim 0.2$ keV associated with regions of current star formation in the disc of NGC 55. After correcting for absorption, the X-ray luminosity of this soft emission is $\sim 4 \times 10^{38}$ erg s⁻¹ (0.3–6 keV).

NGC 55 is categorised as a Magellanic-type dwarf galaxy. From a comparison of its properties with those of other nearby Magellanic systems, specifically the LMC and NGC 4449, we conclude that, from a high energy perspective, NGC 55 is quite typical of its class.

ACKNOWLEDGMENTS

This work is based on observations obtained with *XMM-Newton*, an ESA Science Mission with instruments and contributions directly funded by ESA member states and the USA (National Aeronautics and Space Administration). The other X-ray data used in this work were obtained from the Leicester Database and Archive Service (LEDAS) at the Department of Physics and Astronomy, University of Leicester. The second Digitized Sky Survey was produced by the Space Telescope Science Institute, under NASA Contract No. NAS 5-26555. This research has also used the NASA/IPAC Extragalactic Database (NED) operated by the Jet Propulsion Laboratory, California Institute of Technology, under contract with NASA, and the SIMBAD database operated at CDS, Strasbourg, France. The authors would also like to thank Kevin Briggs for helpful advice regarding source detection techniques and stellar X-ray emission. AMS and TPR gratefully acknowledge funding from PPARC. Finally we thank the referee, Dr Wolfgang Pietsch, for providing a thorough and informative review of our original manuscript.

REFERENCES

- Barber, C. R., Roberts, T. P., & Warwick, R. S. 1996, *MNRAS*, 282, 157
- Beasley M. A., Sharples R. M., 2000, *MNRAS*, 311, 673
- Bomans D. J., Chu Y., Hopp U., 1997, *AJ*, 113, 1678
- Dahlem M., Weaver K.A., Heckman T.M., 1998, *ApJS*, 118, 401
- Davidge T. J., 2005, *ApJ*, 622, 279
- de Vaucouleurs G., 1961, *ApJ*, 133, 405
- de Vaucouleurs G., Freeman K. C., 1972, *VA*, 14, 163
- de Vaucouleurs G., de Vaucouleurs A., Corwin H. G., Buta R. J., Paturel G., Fouque P., 1991, *trcb.book*,
- Dewangan G. C., Griffiths R. E., Choudhury M., Miyaji T., Schurch N. J., 2005, *ApJ*, 635, 198
- Di Stefano R., Kong A. K. H., 2003, *ApJ*, 592, 884
- Di Stefano R., Kong A. K. H., 2004, *ApJ*, 609, 710
- Engelbracht C. W., et al., 2004, *ApJS*, 154, 248
- Fabbiano G., Krauss M., Zezas A., Rots A., Neff S., 2003, *ApJ*, 598, 272
- Feng H., Kaaret P., 2005, *ApJ*, 633, 1052
- Ferguson A. M. N., Wyse R. F. G., Gallagher J. S., 1996, *AJ*, 112, 2567
- Giacconi, R., et al., 2001, *ApJ*, 551, 624
- Gilfanov, M., Grimm H.-J., Sunyaev, R. 2004, *MNRAS*, 347, L57
- Graham J. A., 1982, *ApJ*, 252, 474
- Greiner J., 2000, *NewA*, 5, 137
- Grimm H.-J., Gilfanov, M., Sunyaev, R. 2003, *MNRAS*, 339, 793
- Güdel M., 2004, *A&ARv*, 12, 71
- Hodge P. W., Kennicutt R. C., 1983, *AJ*, 88, 296
- Hummel E., Dettmar R.-J., Wielebinski R., 1986, *A&A*, 166, 97
- Jenkins L. P., Roberts T. P., Warwick R. S., Kilgard R. E., Ward M. J., 2004, *MNRAS*, 349, 404
- Jenkins L. P., Roberts T. P., Warwick R. S., Kilgard R. E., Ward M. J., 2005, *MNRAS*, 357, 401
- Karachentsev I. D. et al., 2003, *A&A*, 404, 93
- Karachentsev I. D. et al., 2004, *ApJS*, 127, 2031
- Kilgard R. E., et al., 2005, *ApJS*, 159, 214
- Kiszkurno-Koziej E., 1988, *A&A*, 196, 26
- Liller W., Alcaïno G., 1983, *ApJ*, 264, 53
- Maddox S. J., Efstathiou G., Sutherland W. J., Loveday J., 1990, *MNRAS*, 243, 692
- Makishima K., Maejima Y., Mitsuda K., Bradt H. V., Remillard R. A., Tuohy I. R., Hoshi R., Nakagawa M., 1986, *ApJ*, 308, 635
- McClintock J. E., Remillard R. A., 2006, in “Compact Stellar X-ray Sources” eds., Lewin W. H. G., van der Klis M., Cambridge University Press, Cambridge, 157
- Miller J. M., Fabbiano G., Miller M. C., Fabian A. C., 2003, *ApJ*, 585, L37
- Mitsuda K., et al., 1984, *PASJ*, 36, 741
- Olsen K. A. G., Miller B. W., Suntzeff N. B., Schommer R. A., Bright J., 2004, *AJ*, 127, 2674
- Oshima T., Mitsuda K., Ota N., Yamasaki N., 2002, *aprm.conf*, 287
- Otte B., Dettmar R.-J., 1999, *A&A*, 343, 705
- Perryman, M. A. C., et al. 1997, *A&A*, 323, L49
- Pietsch W., et al., 2001, *A&A*, 365, L174
- Pietsch W., Misanovic Z., Haberl F., Hatzidimitriou D., Ehle M., Trinchieri G., 2004, *A&A*, 426, 11
- Pietsch W., Freyberg M., Haberl F., 2005a, *A&A*, 434, 483
- Pietsch W., Fliri J., Freyberg M. J., Greiner J., Haberl F., Riffeser A., Sala G., 2005b, *A&A*, 442, 879
- Prestwich A. H., Irwin J. A., Kilgard R. E., Krauss M. I., Zezas

- A., Primini F., Kaaret P., Boroson B., 2003, *ApJ*, 595, 719
- Pritchett C. J., Schade D., Richer H. B., Crabtree D., Yee H. K. C., 1987, *ApJ*, 323, 79
- Protassov R., van Dyk D. A., Connors A., Kashyap V. L., Siemiginowska A., 2002, *ApJ*, 571, 545
- Ranalli, P., Comastri, A., Setti, G., 2003, *A&A*, 399, 39
- Rappaport S., Di Stefano R., Smith J. D., 1994, *ApJ*, 426, 692
- Read A. M., Ponman T. J., Strickland D. K., 1997, *MNRAS*, 286, 626
- Roberts T. P., 1997, PhD thesis, Leicester University
- Roberts T. P., Warwick R. S., Ward M. J., Goad M. R., Jenkins L. P., 2005, *MNRAS*, 357, 1363
- Robinson B. J., van Damme K. J., 1966, *AuJPh*, 19, 111
- Sasaki, M., Haberl, F., Pietsch, W., 2002, *A&A*, 392, 103
- Schlegel E. M., Barrett P., Singh K. P., 1997, *AJ*, 113, 1296
- Shectman, S. A., Landy, S. D., Oemler, A., Tucker, D. L., Lin, H., Kirshner, R. P., & Schechter, P. L. 1996, *ApJ*, 470, 172
- Solano E., Garrido R., Fernley J., Barnes T. G., 1997, *A&AS*, 125, 321
- Stark A. A., Gammie C. F., Wilson R. W., Bally J., Linke R. A., Heiles C., Hurwitz M., 1992, *ApJS*, 79, 77
- Stobbart A.-M., Roberts T. P., Warwick R. S., 2004, *MNRAS*, 351, 1063
- Stobbart A.-M., Roberts T. P., Wilms J., 2006, *MNRAS*, 368, 397
- Strüder L., et al., 2001, *A&A*, 365, L18
- Summers L. K., Stevens I. R., Strickland D. K., Heckman T. M., 2003, *MNRAS*, 342, 690
- Strickland D. K., 2004, *IAUS*, 222, 249
- Thronson H. A., Hunter D. A., Telesco C. M., Decher R., Harper D. A., 1987, *ApJ*, 317, 180
- Tikhonov N. A., Galazutdinova O. A., Drozdovsky I. O., 2005, *A&A*, 431, 127
- Tüllmann R., Rosa M. R., Elwert T., Bomans D. J., Ferguson A. M. N., Dettmar R.-J., 2003, *Msngr*, 114, 39
- Tüllmann R., Rosa M. R., 2004, *A&A*, 416, 243
- Turner M. J. L., et al., 2001, *A&A*, 365, L27
- van den Heuvel E. P. J., Bhattacharya D., Nomoto K., Rappaport S. A., 1992, *A&A*, 262, 97
- Van de Steene G.C., Jacoby G.H., Praet C., Ciardullo R., Dejonghe H., 2004, *astro-ph/0407348*
- Vogler A., Pietsch W., 1997, *A&A*, 319, 459
- Wang Q., Hamilton T., Helfand D. J., Wu X., 1991, *ApJ*, 374, 475
- White N. E., Giommi P., Angelini L., 2000, *yCat*, 9031, 0
- Willingale R., Hands A. D. P., Warwick R. S., Snowden S. L., Burrows D. N., 2003, *MNRAS*, 343, 995
- Wilms J., Allen A., McCray R., 2000, *ApJ*, 542, 914